Iron oxide nanoparticles as carriers for the Dy-166/Ho-166 in vivo generator

A study into the characteristics and retention of Dy and Ho in iron oxide nanoparticles

LO 4

Linge Dicke

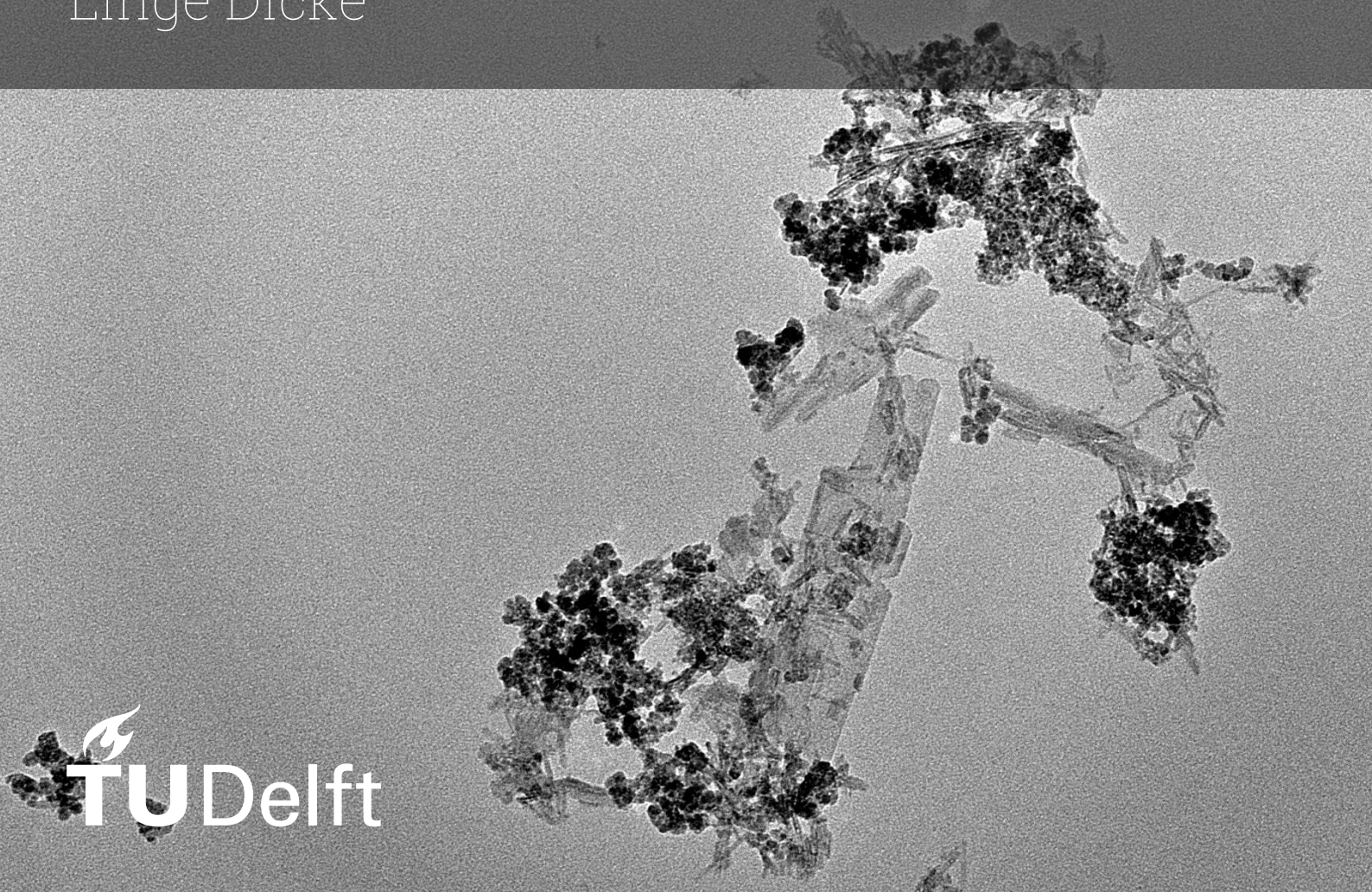

TU Delft

Iron oxide nanoparticles as carriers for the Dy-166/Ho-166 in vivo generator

A study into the characteristics and retention of Dy and Ho in iron oxide nanoparticles

by

Linge Dicke

to obtain the degree of Bachelor of Science for Molecular Science and Technology at the Delft University of Technology, to be defended on Friday 27, 2023 at 09:30.

Course:	LO4
Student Number:	5188725, s2597756
Supervisor:	Antonia G. Denkova
Daily supervisor:	Runze Wang
Thesis Committee:	Antonia G. Denkova, Kristina Djanashvili
Project Duration:	September 2022 - January 2023

Cover: An image made with a transmission electron microscope of dysprosium doped iron oxide nanoparticles synthesized during this thesis.

TU Delft

Preface

This thesis shows a research performed for the Bachelor end project, also called LO4, in the Applied Radiation & Isotopes group of the department of Radiation Institute Delft of TU Delft's Faculty of Applied Sciences.

I would like to thank Runze Wang (PhD candidate) for allowing me to work with him and being my daily supervisor throughout this project in and out of the laboratory. I would also like to thank my supervisor Antonia G. Denkova for giving me this amazing opportunity to work on this project. At last I want to thank all the members the ARI reserach group and technicians who have helped me during by thesis. I started this research with a hand injury which made it a bit more difficult, with the help I got from all the people mentioned above I still had a very nice experience and I was able to finish my thesis.

Linge Dicke
Delft, January 2023

Contents

List of Figures

List of Tables

Abstract

Background:
Cancer is one of the leading causes of death worldwide. Targeted radionuclide therapy has become a important treatment, this is when a carrier molecule is attached to a radionuclide to deliver cytotoxic radiation levels to diseased cells. β^- emitters are frequently used in RNT because they have a long penetration depth, such as the dysprosium-166/holmium-166 (^{166}Dy/^{166}Ho) in vivo generator. The ^{166}Dy/^{166}Ho in vivo generator shows great potential for large tumors because of the long half-life time of the mother nuclide ^{166}Dy and the emission of high energy β^- from the daughter nuclide ^{166}Ho. Previous research shows the release of 72 % of the ^{166}Ho when ^{166}Ho is bound to conventional chelators due to internal conversion after the β^- decay. The aim of this thesis is to synthesize an iron oxide nanoparticle as carrier for the ^{166}Dy/^{166}Ho in vivo generator. This iron oxide nanoparticles (SPIONs) should prevent internal conversion and thus the loss of the daughter nuclide ^{166}Ho.

Results:
The dysprosium doped iron oxide nanoparticles were synthesized successfully with an average diameter of 6.1 ± 1.5 nm, measured with TEM. The DLS and TEM results showed that the SPIONs were aggregating. The labeling efficiency represents how much Dy is retained in the Dy doped SPIONs, for the non-radioactive Dy this was measured with the ICP/OES. The labelling efficiency was 3.21 ± 0.8 %. The ^{166}Dy doped iron oxide nanoparticles were also synthesized successfully with a radiolabelling efficiency of 3.12 ± 2.2 %, measured with a 2480 Wizard 2 Gamma counter. The retention of ^{166}Dy $+ ^{166}$Ho was 79.2 ± 1.8 % after 96 h.

Conclusion:
The retention of ^{166}Dy $+ ^{166}$Ho in iron oxide nanoparticles was 79.2 ± 1.8 % after 96 hours. This is much higher than the retention of 28% by conventional chelators. This means that the iron oxide nanoparticls is a safer carrier for the ^{166}Dy/^{166}Ho in vivo generator than the conventional chelator.

Nomenclature

Abbreviations

Abbreviation	Meaning
CPM	counts per minute
DLS	Dynamic light scattering
DPTA	Diethylenetriamine pentaacetate
Dy-SPIONs	Dysprosium doped superparamagnetic iron oxide nanoparticles
EDTA	Ethylenediaminetetraacetic acid
Fe	Iron
H_2SO_4	Sulfuric acid
ICP/OES	Inductively coupled plasma/optical emission spectroscopy
MW	molecular weight
NaI	Sodium iodine
NaOH	Sodium hydroxide
NP	Nanoparticle
PEG	Polyethylene glycol
rfc	Relative centrifugal force
RNT	Radionuclide therapy
rpm	Rotations per minute
SPION	Superparamagnetic iron oxide nanoparticles
TEM	Transmission electron microscopy
TEOS	Tetraethylorthosilicate
γ-Fe_2O_3	Maghemite
^{166}Dy	Dysprosium-166
^{166}Ho	Holmium-166
^{166}Dy-SPIONs	Dysprosium-166 doped superparamagnetic iron oxide nanoparticles

Symbols

Symbol	Meaning
eV	Electronvolt
λ	Decay constant
N	Amount of atoms of nuclide
A	Activity
t_{Z+1}	Half-life

1 Introduction

Cancer is one of the leading causes of death in the world. In 2020 nearly 9,6 million deaths were estimated to be caused by cancer and these numbers are expected to increase [1]. Cancer is a disease in which some of the body's cells grow uncontrollably and spread to other parts of the body shutting down normal organ functions. There are many forms of cancer and various stages of growth and therefore diverse treatment is needed. The main goal of cancer treatment is to cure cancer, if this is not possible the goal of the treatment is to prolong life. The most common treatments for cancer are: surgery, radiotherapy and systemic therapy [1]. Systemic therapy is preferred for cancer in the metastases and it includes chemotherapy, hormonal treatments, targeted biological therapies and radionuclide therapy (RNT) [1],[2].

RNT is defined by how the radioactive atoms are delivered to tumour-associated targets. RNT uses a carrier molecule attached with a radionuclide to deliver cytotoxic radiation levels to disease cells. Once distributed to the tumor site, the ionizing radiation emitted by the radionuclides can damage the DNA of the cancer cells and lead to apoptosis. This way the cancer cells are reduced. RNT is usually performed in fractions, this means that multiple injections are given with a time interval of a couple days. This way the cancer cells are reduced and the healthy cells remain. Also side effects are generally less severe than with chemotherapy [3]. Nanoparticles (NPs) recently drew attention as radionuclide carriers for RNT [4]. β^- emitters are frequently used in RNT due to the long tissue penetration depth of the β^- particles [5].

In this thesis the dysprosium-166/holmium-166 (^{166}Dy/^{166}Ho) in vivo generator will be researched for RNT use. ^{166}Ho is the daughter radionuclide of ^{166}Dy. ^{166}Dy has a relatively long half-life time of 26.8 h and ^{166}Ho emits high β^- energy 1.7 to 1.85 MeV. These two advantages combined are the reason that the ^{166}Dy/^{166}Ho in vivo generator is a promising option for RNT. The ^{166}Dy/^{166}Ho in vivo generator shows great potential for treating large tumors, but the internal conversion occurring after β^- decay from ^{166}Dy to ^{166}Ho is still a problem. The internal conversion causes a release up to 72 % of ^{166}Ho when ^{166}Dy is bound to conventional chelators [5]. With the right nanoparticle as radionuclide carrier this can be reduced and the ^{166}Dy/^{166}Ho in vivo generator will be safer.

1.1. Aim of thesis

The aim of this thesis is to develop a nanoparticle based carrier for ^{166}Dy/^{166}Ho in vivo generator which will prevent the loss of the daughter nuclide ^{166}Ho induced by internal conversion. Iron oxide nanoparticles could be a possible carrier, because they can bond with ^{166}Dy and possibly keep they ^{166}Ho inside. Iron oxide nanoparticles already showed promising results as carrier for ^{99}Tc and ^{188}Re, so during this research several experiment will be done to see if iron oxide nanoparticles will also be good carriers for the ^{166}Dy/^{166}Ho in vivo generator [6].

The experiments are divided into two parts. This first part will be non-radioactive and it will focus on finding out what the influence is on size and labeling efficiency when Dy is incorporated into the iron oxide nanoparticles. Therefore the first research question is:

What is the influence of incorporating Dy in iron oxide nanoparticles on the size and what is the labelling efficiency of Dy in the iron oxide nanoparticles?

In the second part, the radioactive part, will be determined if iron oxide nanoparticles are indeed good carriers by finding out the retention of the ^{166}Dy doped iron oxide nanoparticles. The second and main research question is:

What is the retention of the daughter nuclide of ^{166}Dy (^{166}Ho) on the ^{166}Dy doped iron oxide nanoparticle carrier?

1.2. Structure of thesis

This thesis will be an explanatory research paper. This introductory chapter stated the importance of this research and the research goals. In chapter 2, background information is given about the materials and the apparatuses that are used for this research. Chapter 3 will show the experimental part. In chapter 4 the results of the experiments will be shown and their meaning will be discussed. In chapter 5 the conclusion of the research is presented and recommendations for possible further research are proposed.

2

Theory

2.1. Targeted radionuclide therapy

As explained in the introduction targeted RNT is a treatment where cytoxtic levels of radiation are delivered to tumors [5]. Cancer cells have specific receptors which only bind to specific targets, allowing only specific species from entering the cell. By reverse engineering this, synthesising these target molecules and binding them to a carrier, allows us to transport the radionuclide inside the cancer cell [7], this is shown on the right side of figure 2.1. This figure also shows that a nanoparticle has a higher payload than a conventional chelators, see the left side of figure 2.1 [8].

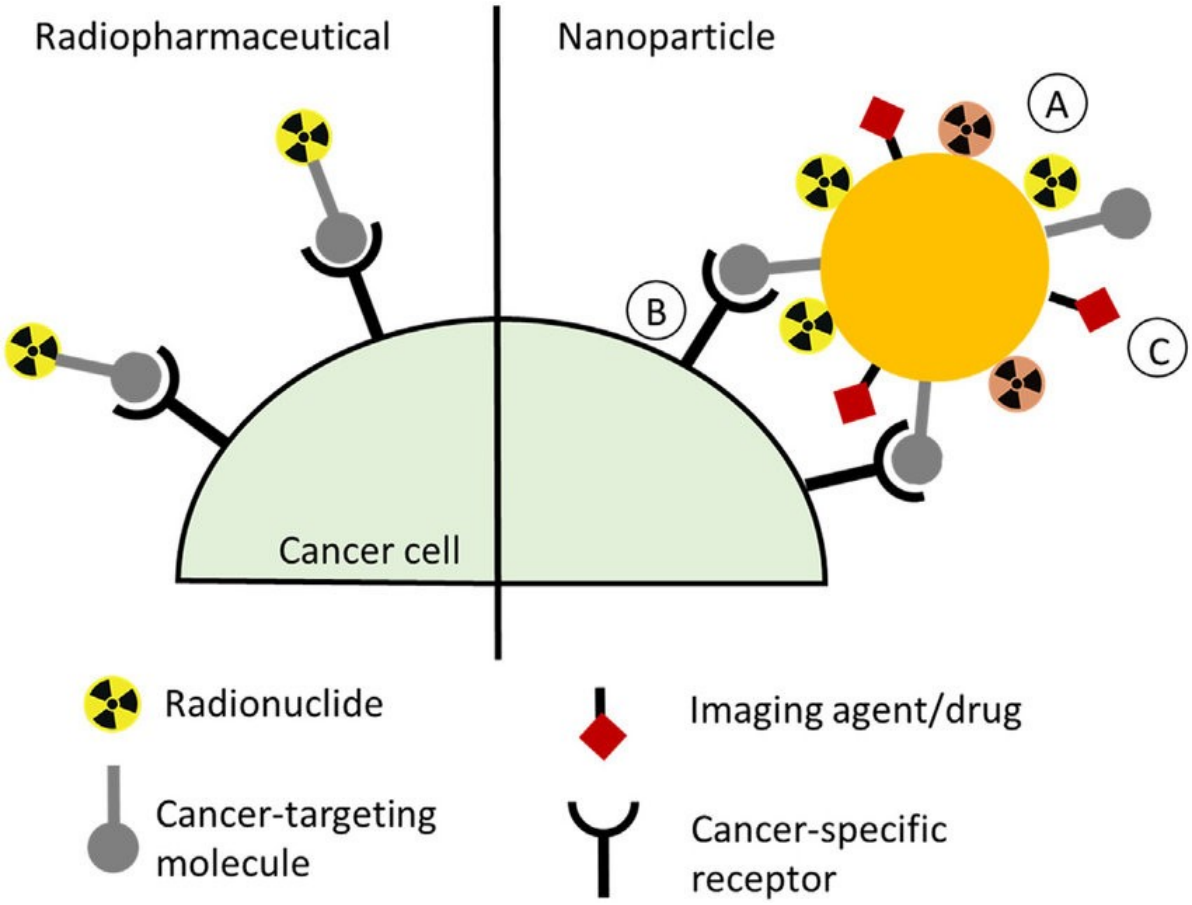

Figure 2.1: A schematic overview of nanoparticles in nuclear medicine [8].

2.1.1. Radioactivity and ionizing radiation

When atoms are unstable they are called radionuclides. Radionuclides have extra protons or neutrons and because of this they have excess energy. The radionuclide has to release this excess energy to become stable. This is done by releasing subatomic particles or electromagnetic radiation from the nucleus or by converting/capturing energy within the atom, collectively known as radioactive decay. The radionuclide produces a daughter nuclide. The radiation emitted is measured in electron volts (eV) [9]. Each isotope has specific probabilities of decay and energy which characterize that isotope.

Ionizing radiation are particles or electromagnetic waves that have sufficient energy to rip electrons from atoms or molecules leaving them ionized. They often have enough energy to damage DNA and destroy living cells. The radiation released from the radionuclide can damage the DNA directly or indirectly. Indirect damage is done by the formation of H_2O radicals. Both pathways will cause the cell to self destruct (apoptosis) or repair possibly causing mutations, see figure 2.2. Mutations increase the possibility of a cell becoming tumorous, however by directing the radiation to unhealthy cells the tumor cells will decrease [10].

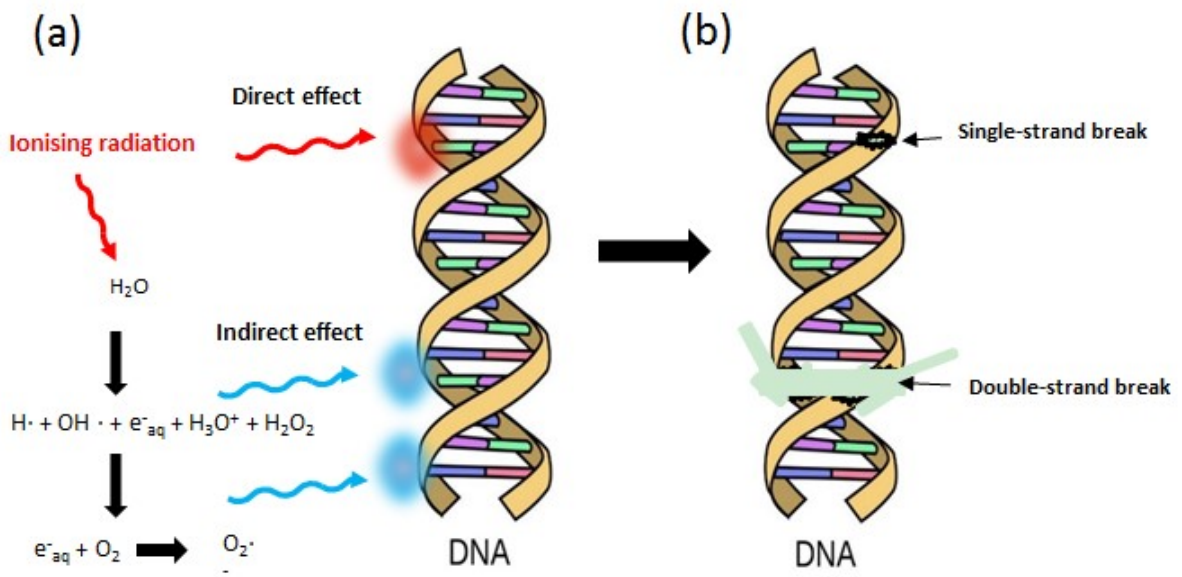

Figure 2.2: Schematic of how ionising radiation can damage DNA. Radiation can directly damage DNA or indirectly damage it through radicals (a). DNA damage can occur as a result of single-strand breaks or double-strand breaks (b) [10].

Radioactive decay is described by the half-life, which is the time for half of the radioactive nuclide to undergo radioactive decay. A radionuclide has a unique decay constant λ, which is related to the half-life, see eqation 2.1 [9]. A radionuclide with an amount of atoms, N, has an amount of atoms that undergoes radioactive decay called activity, A, see eqation 2.2. The activity of a source is described in Becquerel (Bq), corresponding to decays per second.

$$\lambda = \frac{\ln(2)}{t_{1/2}} \tag{2.1}$$

$$A = \frac{\delta N(t)}{\delta(t)} = \lambda * N(t) \tag{2.2}$$

A nucleus can decay via the following processes, α decay, β^- decay, β^+ decay, electron capture, isomeric transition and spontaneous fission. The nucleus can also release energy via internal conversion. For this project only β^- will be discussed since it is the most important type of decay for the ^{166}Dy/^{166}Ho in vivo generator. β^- decay occurs when a radionuclide's nucleus emits an electron, also called a β^- particle, an antineutrino and energy, see equation 2.3 [9]. How far a β^- can travel depends on the energy and the surrounding matter it interacts with. The particles have a range between 0.9 and 5.0 MeV [9].

$$ {}^{A}_{Z}\mathrm{N} \rightarrow {}^{A}_{Z+1}N' + {}^{0}_{-1}\beta^- + {}^{0}_{0}\bar{\nu} + \mathrm{Q}^- \tag{2.3} $$

2.1.2. Previous work on Dy-166/Ho-166 in vivo generator

Dysprosium has seven naturally occurring isotopes and more than 40 radioisotopes with corresponding daughter nuclides. One of those daughter nuclides is Holmium-166 (^{166}Ho), which will be used in this research. ^{166}Ho can be produced by two methods; neutron activation by irradiation in a nuclear reactor or with a ^{166}Dy/^{166}Ho in vivo generator. Both production ways are shown in figure 2.3. The in vivo generator concept in radiotherapy has a mother nuclide with an intermediate half-life and intermediate energy. This mother nuclide decays to a daughter nuclide with a short half-life and high energy. With the in vivo generator the half-life and the β^- energy are both increased. These two advantages combined make the in vivo generator promising for RNT. The ^{166}Dy/^{166}Ho in vivo generator will be used in this research. ^{166}Dy has a half-life time of 81.6 h and decays to ^{166}Ho via β^- decay [11]. ^{166}Ho is a β^- emitter that decays to ^{166}Er and emits β^- particles with maximum energy of 1.85 MeV and this results in a maximum tissue penetration depth of 8.7 mm [12].

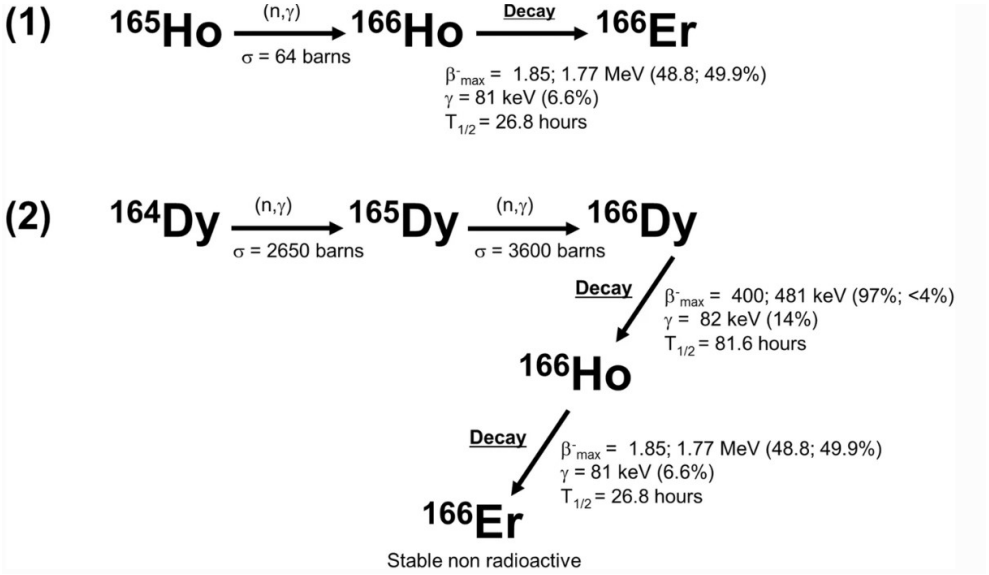

Figure 2.3: Schematic of the production methods of ^{166}Ho with the energy and probability of the radiation types. (1) reactor neutron activated ^{166}Ho and (2) with a ^{166}Dy/^{166}Ho in vivo generator [12].

The ^{166}Dy/^{166}Ho in vivo generator has potential to kill tumors. Several carriers have been loaded or conjugated to this in vivo generator such as antibodies, micro particles, organic complexes and liposomes [12]. As mentioned in chapter 1, the ^{166}Dy/^{166}Ho in vivo generator has been researched as a potential carrier, but up to 72 % of the ^{166}Ho was released when DOTA was used as chelator [13]. This was because 72 % of ^{166}Dy decays by internal conversion leading to an auger cascade during which the ^{166}Ho atom becomes highly positive for a short period. The binding electrons from the complex are taken in by the highly positive ^{166}Ho-ion and then the complex will collapse, freeing ^{166}Ho caused by electrostatic repulsion. The loss of the radioactive nuclides will cause harm in the body to the healthy cells [13]. Iron oxide nanoparticles could be a possible carrier, because they can bond with ^{166}Dy and possibly keep the ^{166}Ho inside.

2.1.3. Iron oxide nanoparticles

Iron (Fe) is a transition metal in group 8 with atomic number 26. Iron has four possible oxidation states: Fe^{2+} and Fe^{3+}, which are the most important, and Fe^{4+} and Fe^{6+}. Iron oxide has tree possible forms: alpha, gamma and delta iron [14]. Gamma iron oxide nanoparticles have continuous fluctuations of the magnetic moment leading to a net zero magnetic moment, this phenomenon is called superparamagnetic. This means that the magnetic response of a iron oxide nanoparticle to an external magnetic field depends mainly on the interaction between uncompensated electron spins and the system's temperature [15]. Superparamagnetic iron oxide nanoparticles (SPIONs) are composed of ferrimagnetic nanocrystals with a spinel structure. Usually, these nanoparticles are metabolized through the liver or through the kidneys, called the hepatobiliary pathway and the renal pathway. SPIONs in the size range 3 nm to 100 nm are already used for medical applications. The nanoparticles in this size range present a unique opportunity to interfere with natural processes involving viruses, bacteria or cells [16].

Even though the SPIONs can pass through the renal or hepatoboliary pathways, still a small fraction of the SPIONs can stay in the body over long periods. The nanoparticles degrade into Fe^{3+} ions and form hemoglobin. Fe^{3+} have low toxicity, but they can still do damage to the human tissue, therefore is it desirable to clear out the particles from the body fast [17]. The diameter of the pores in small blood vessels in the kidney, called glomerular capillaries, is 5.5 nm to 10 nm [18]. The average particle size of the SPIONs needs to be smaller than 5.5 to pass through the renal system [19].

Maghemite (γ-Fe_2O_3) is an SPION. It is a stable polymorph with an inverse spinel structure where all 3 iron cations are occupied, called the trivalent state. The inverse spinel structure possesses an antiferromagnetic coupling between the tetrahedral sites (site-A) and the octahedral sites [20]. The unit cell of maghemite can be written as $(Fe^{3+})[\square_{1/6}\, Fe_{5/6}{}^{3+}]_2\, O_4$ where the brackets ( ) represents the A-site, the [ ] is the B-site and the square $\square$ represent the empty spaces. A cell which describes this same crystal, but with a larger volume is called a a supercell. A supercell can be made of maghemite, with c/a = 3, which will make the maghemite system completely ordered. Then, the lattice constant can be set to $8.347 * 8.347 * 25.042$ Å and then it forms a supercell with 160 atoms. The unit cell of maghemite can now be written as $(Fe^{3+})_{24}[\square_8\, Fe_{403}{}^{3+}]\, O_{96}$. Figure 2.4 shows the γ-Fe_2O_3 supercell [17]. These nanoparticles (NPs) posses good uniformity, dispersity and crystallinity with an ultrasmall size of 5.3 nm [17]. A particle with this size can be cleared by the human body itself trough the renal system and is therefore not toxic for humans [19]. The chemical reaction to produce these SPIONs is shown in equation 2.4 [21].

$$Fe_2{}^{+} + 2\, Fe_3{}^{+} + 8\, OH \rightarrow \gamma - Fe_3O_4 + 4\, H_2O \tag{2.4}$$

These maghemite SPIONs can be incorporated with Dy and ^{166}Dy. Adding trace levels of radioactive precursors together with normal non-radioactive precursors during the synthesis of nanoparticles is a simple and straightforward. With this method, radioisotopes can be well embedded into the crystal lattice of final nanocrystals, resulting in radioactive nanoparticles with high stability [22]. Adding a layer of Polyethyleenglycol (PEG) to SPIONs can improve the blood circulation half-life and thus the tumor uptake of the NPs [23].

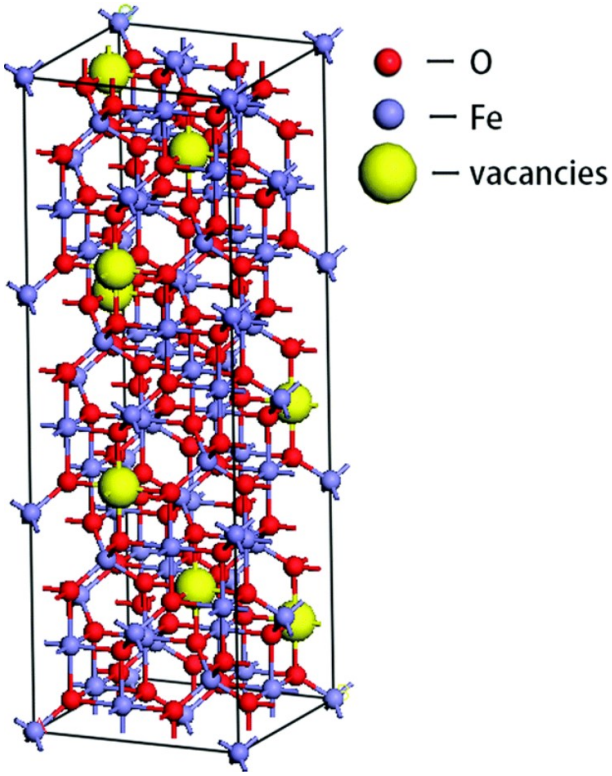

Figure 2.4: The inverse spinel structure of the γ-Fe_2O_3 supercell [17].

2.2. Apparatuses

To answer the research questions stated in chapter 1.1 numerous apparatuses were used for data collection. The function of the used apparatus are explained in this section.

2.2.1. Inductively Coupled Plasma Optical Emission spectroscopy

Inductively coupled plasma/optical emission spectroscopy (ICP/OES) is an apparatus that determines metals in a variety of different sample matrices [24]. With this technique, liquid samples are injected with devices that produce a fine spray of liquid, nubilizers, into a radiofrequency-induced argon plasma. The sample mist reaching the plasma is quickly dried, vaporized, and energized through collisional excitation at high temperature [25]. The atomic emission flowing from the plasma is collected with a lens and imaged onto the entrance slit of a wavelength selection device [26]. In figure 2.5 is a schematic of an ICP/OES is shown.

Atoms can absorb energy to excite electrons to a higher energy level. The principle of the ICP/OES uses the transition of electrons from a higher energy level to a lower energy level, these excited atoms then release energy. This energy is the form of light photons of a specific wavelength, which is unique to each atom. These wavelengths are cross references with a database to determine the element type. The number of atoms transitioning to a higher energy state is proportional to the sum of light emitted at each wavelength [27].

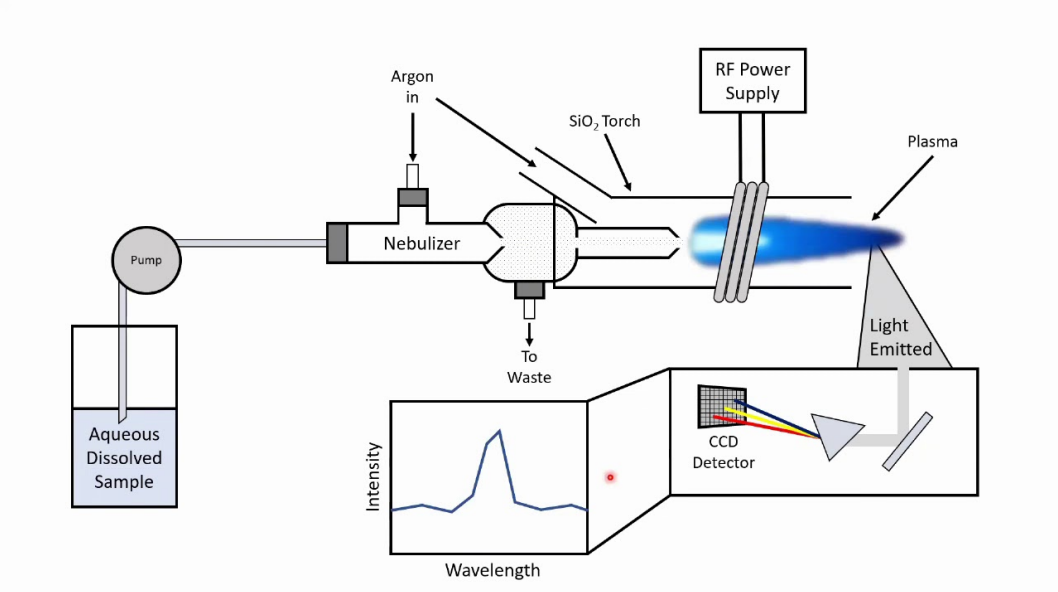

Figure 2.5: Schematic of the components of an ICP/OES [24].

2.2.2. Dynamic Light Scattering

Dynamic light scattering (DLS) measures time-dependent fluctuations in the scattering intensity from particles undergoing a Brownian motion [28]. Shining a laser onto a solution with spherical particles in Brownian motion shifts the light when it hits the moving particle and thus changing the wavelength of the incoming light, see figure 2.6 a. This change in waveleghth is related to the size of the particle [29]. By using the autocorrelation function it is possible to compute the diffusion coefficient and by using the Stokes-Einstein equation it possible to calculate the hydrodynamic size of the particles in the solution, see figure 2.6 b [30].

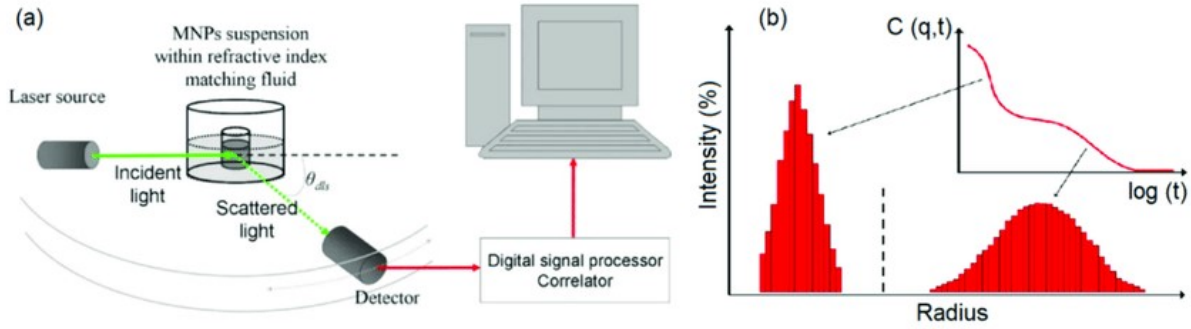

Figure 2.6: A schematic of the DLS setup (a). The acquired results from the DLS set-up (b) [30].

2.2.3. Transmission Electron Microscopy

Nanoscale structures are difficult to be resolved by conventional light microscopy. Transmission electron microscopy (TEM) uses electrons to create images of samples. TEM has been widely used for caracterization of morphology, crystalline structures, and elemental information of membrane materials. TEM can create images of particles around 100 nm and can thus be used for the SPIONs of this thesis [31]. In figure 2.7 a schematic of a TEM is shown. An electron gun generates electron beams. These beams are sent through a column in which only a very specific wavelength can pass, which generates a well-defined beam. The transmitted electrons are sent trough the sample and then various fluorescent lenses, such as condenser, objective, and projective lens. The beam is then projected on a phosphor screen to convert the electron image [31].

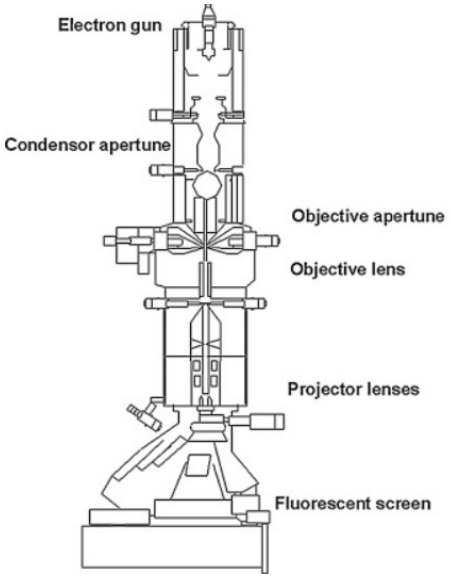

Figure 2.7: Schematic of the outline of an TEM [31].

2.2.4. Gamma Counter

A gamma counter is a type of solid scintillation counter that measures ionizing radiation [32]. Gamma counters do just as the name implies, they quantify the activity of a γ-emitting sample. A crystal of sodium iodine (NaI) surrounds the sample and uses incident radiation to generate photons [33]. These photons are measured using a sensitive photo multiplier tube. A photo multiplier tube uses the photoelectric effect, this occurs when a photon hits the photocathode and an electron is produced. The electron is multiplied via a chain of dynodes by a process called secondary emission, a phenomenon where a second particle is emitted when the electron hits the dynode. The electrons are also accelerated by a high voltage field to the rear of the photomultiplier tube. This produces enough electrons to send a voltage pulse. The end of the photomultiplier tube is connected to electronic equipment to analyse the voltage pulse across an external resistor. The magnitude of the voltage pulse is proportional to the intensity of the photon, these pulses are calculated to counts per minute [32].

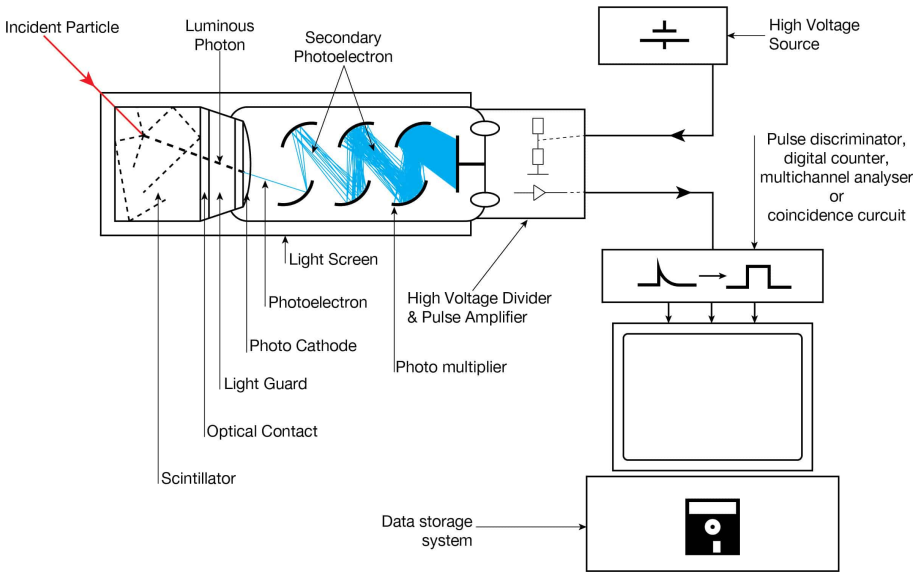

Figure 2.8: Schematic of the components of a gamma counter [32].

3

Methods and Materials

This chapter will list all the chemicals, materials, equipment and apparatuses used in the experiments. This chapter will also describe the method for the synthesis of the Dy-SPIONs and how the apparatuses were used.

3.1. Chemicals

Table 3.1 shows the chemicals used in the experiments. The volumes, mass, concentrations, purity and supplier of the product are given.

Table 3.1: Chemicals used in experiments.

Material	Volume / Mass	Concentration [M]	Purity [%]	Supplier
MilliQ water	50 - 200 mL	-	-	MilliQ A10
$FeCl_2 \cdot 4\,H_2O$	1.75 g	0.175	98	Sigma-Aldrich
$FeCl_3 \cdot 6\,H_2O$	3.5 g	0.25	98	Sigma-Aldrich
H_2SO_4	20 µL	Concentrated	$95 - 97$	Sigma-Aldrich
NaOH	2.8 g	1	97	Sigma-Aldrich
PEG-bis(carboxymethyl)ether	1 mL, 1 wt%	-	99	Sigma-Aldrich
DSPE-PEG(2000) Carboxylic Acid	1 mL, 1 wt %	-	99	Avanti
EDTA	20 µL	0.1	99	Sigma-Aldrich
PDTA	20 µL	0.1	99	Sigma-Aldrich
HCl 30 %	10 mL	12	97	Sigma-Aldrich
$Dy(NO_3)_3 \cdot 5\,H_2O$	122 mg	0.015	99.99	Alfa Aesar

3.2. Equipment and apparatuses

Table 3.2 and 3.3 show the apparatuses and equipment used during the experiments. The most important parameters and/or the model is noted. The table also lists all the suppliers of the equipment. Later in this chapter is explained exactly how the apparatuses are used.

Table 3.2: Apparatuses used in experiments.

Apparatus	Parameters	Supplier
DLS	35 mW laser, ALV sp s/w 93 goniometer	TU - Delft
JEM-1400 Plus Electron microscope	120 kV	JEOL
Optima 5300 DV (ICP)	$300 - 800$m	Perkin Elmer
2480 Wizard 2 Gamma counter	-	Perkin Elmer

Table 3.3: Equipment used in experiments.

Equipment	Parameter/model	Supplier
Pipettes	10 µL to 5000 µL	Gilson and Biohit
Pipettes tips	10 µL to 5000 µL	Greiner bio-one
Syringe	30 mL	BD plastipak
Sonicator	$40\,^{\circ}$C to$50\,^{\circ}$C	Branson
Plastic vial	50 mL	Sarsted
Round bottom flask	100 mL	VWR
Syringe pump	$21,59$ mm, $2,5$ mL/min, 25 mL	World precision instruments
Beaker	25 mL to 500 mL	Pyrex
Tube	1.5 mL	Eppendorf
Oven	$60\,^{\circ}$C	Venticell Eco line
Centrifugion	21300 rcf, centrifuge 5425	Eppendorf
Magnetic stirrer	300 rpm, RW 16 basic IKA	IKA
Labaratorium hot plate	$60\,^{\circ}$C	Stuart Equipment
Fumehood	-	TU-Delft
Vortex	Vortex Genie 2 Mixer	Geneo
Lead bricks	-	TU-Delft
Plastic shielding	-	TU-Delft
Syringe filter	0.22 µm	BGB
Syringe	1 mL	Braun
pH indicator paper	pH = $1-11$,	Avantor

3.3. Non-radioactive experiment

3.3.1. Sysnthesis of Dy doped SPIONs

The following method was used to produce iron oxide nanoparticles. This synthesis was adapted from the paper of Yin et al. from 2019 with some small changes [17]. 25 mL of milliQ water, 1.75 g of $FeCl_2 \cdot 4\,H_2O$ and 3.5 g of $FeCl_3 \cdot 6\,H_2O$ were added to a round bottem flask. Then 20 µL of concentrated H_2SO_4 was added. The flask was placed on a hot plate with the flask in silica gel and the plate was set to $60\,^{\circ}$C. The solution was thoroughly mixed for 30 min using an a mechanic or magnetic stirrer at 300 rpm. 2.8 g of NaOH was dissolved in 25 mL MilliQ water. The NaOH solution was transferred into a syringe pump with an attached tube and with this syringe pump the speed of the titration could be regulated. The speed was set to $2,5$ mL/min. The syringe pump was placed next to the round bottom flask and the titration was started with a total duration of 15 min. There were batches of SPIONs made with and without Dy incorporated. 122 mg $Dy(NO_3)_3 \cdot 5\,H_2O$ was put in 50 mL water. The Dy doped SPIONs (Dy-SPIONs) were made by adding the solution with the Dy source into the reaction solution during the titration of NaOH. Half of the Dy source was added after 5 min and half was added after 10 min with a pipette. After the complete addition of the $Dy(NO_3)_3 \cdot 5\,H_2O$ and the NaOH solution, 1 mL of 1 wt% PEG-bis(carboxymethyl)ether was added to the flask and the reaction was continued for 30 minutes. Then the solution in the flask was transferred into a beaker and cooled down to room temperature.

3.3.2. Sample characterization

Measurements with ICP-OES, DLS and TEM were used to determine the characteristics of the iron oxide nanoparticles. The following sections will give the required different preparations before each measurement and the settings of the apparatuses.

DLS

The hydrodynamic radius was measured using DLS. The DLS apparatus is made of a JDS Uniphase 633 nm 35 mW laser, an ALV sp s/w 93 goniometer, a fibre detector and a photon counter from Perkin Elmer. Toluene was used as the index-matching fluid. The samples were diluted 100 times and then centrifuged for 30 min at 21300 rcf and the supernatant was decanted. 1 mL of milliQ was added to the sample, this process of centrifuging and decanting was repeated twice to make sure the solution was

washed properly. After washing the samples were placed in a sonicator at $50\,^{\circ}$C for 90 min [5].

TEM
The morphology and size of the SPIONs was inspected with a JEM-1400 Plus transmission electron microscope from JEOL at the acceleration voltage of 120 kV [5]. The software ImageJ was used on the TEM images for further dertermination of the size. 15 µL was taken from the samples already prepared for the DLS and used for TEM.

ICP/OES
The Dy^{3+} and Fe^{3+} concentrations as well as the doping amounts of the samples were determined by ICP/OES. Before the sample measurements, the ICP/OES was calibrated using standard solutions of known Dy and Fe concentrations. The samples were prepared the following method.1 mL samples of the Dy-SPIONs were taken and weighted in Eppendorf. The samples were washed with water and then they were centrifuged for 30 min at 21300 rcf. As much supernatant as possible was removed and the resulting product was placed into a vacuum drying oven, dried at $60\,^{\circ}$C overnight to obtain the desired dry Dy doped SPIONs. After the weighing 1 mL of 30 % HCl was added to the precipitate and left over night to make sure the SPIONs were fully dissolved. 100 µL was pipetted into a tube and filled up to 10 mL with 3% HCl. The solution was left over night again to ensure well solved samples. The presence of Dy was measured at a wavelength of 353.170 nm, 364.540 nm and 394.468 nm. The presence of Fe was measured at 238.204 nm, 239.562 nm and 259.939 nm. The labelling efficiency was calculated with formula 3.1. $[Dy_{ICP/OES}]$ was the concentration of dysprosium left in the sample after washing 3 times with milliQ and $[Dy_{synthesis}]$ was the amount of Dy added during the synthesises.

$$labelling\ efficiency\ [\%] = \frac{[Dy_{ICP/OES}]}{[Dy_{synthesis}]} * 100\% \tag{3.1}$$

3.3.3. Sample optimization

The Dy-SPIONs were synthesized and characterised in water. The dispersion of the Dy-SPIONs in water was tried to be optimized in 5 different ways:

1. Synthesizong the Dy-SPIONs with another PEG: DSPE-PEG(2000) Carboxylic Acid. The procedure was the same as with the PEG-bis(carboxymethyl)ether.
2. The amount of PEG-bis(carboxymethyl)ether was doubled, so 2 mL of 1 wt% was added during the synthesis.
3. The pH of the solution of the SPIONs was changed. A solution of 1 M NaOH was made and it was diluted with the gradient dilution method to 6 new solutions with pH $14, 13, 12, 11, 10, 9, 8$. The same was done with HCl and solutions with pH 4 and 5 were prepared. The samples were centrifuged and then instead of adding milliQ, these new base or acid solutions were added to the samples. They were all sonicated at $50\,^{\circ}$C for 2 h and then measured with DLS.
4. A fourth method was used to optimize the dispersion of the SPIONs: before adding the PEG-bis(carboxymethyl) ether the Dy doped SPIONs were sonicated. Sonication was combined with scaling down the synthesis. Two solutions of 10 mL were taken from the well-mixed reaction solution. One solution was sonicated at at $40\,^{\circ}$C for 60 min and the other solution was sonicated for 90 min. After the sonication 1 mL of 1 wt% PEG was added and the solution was heated again at $60\,^{\circ}$C in silicon oil. After this the solution was cooled down to room temperature as was done for the other solutions.
5. The Dy-SPIONs were filterd using a 1 mL syringe pushing the solution through a 0.22 µm syringe filter. Then the samples were measured with DLS. After 7 days the samples were measured again.

3.4. Radioactive experiment

The following method was used to produce and examine iron oxide nanoparticles incorporated with Dy^{3+} using a radioactive solution of $Dy(NO_3)_3 \cdot 5\,H_2O$. The experiments with radioactive Dy are adapted from the paper of Wang et al. from 2022 with some small changes.

3.4.1. Production of Dy-166

^{166}Dy was produced by the double neutron capture reaction of ^{164}Dy as described in section 2.1.3. 15 mg $Dy(NO_3)_3 \cdot 5\,H_2O$ powder was irradiated in the nuclear reactor research facility (HOR, Hoger Onderwijs Reactor) at the Department of Radiation Science and Technology of the Delft University of Technology (Delft, the Netherlands) [5]. It was irradiated for 10 h. During the irradiation, the thermal flux was $4.89 * 10^{16}$ s^{-1} m^{-2}. The epithermal flux was $9.3 * 10^{14}$ s^{-1} m^{-2} and the fast flux was $3.75 * 10^{15}$ s^{-1} m^{-2}. After the irradiation it was dissolved in 5 mL milliQ.

3.4.2. Synthesis of radioactive Dy-166 doped iron oxide nanoparticle

350 mg non-radioactive $Dy(NO_3)_3 \cdot 5\,H_2O$ was added and together with 36.5 mL milliQ to the radioactive solution to make a stock solution for 3 batches of ^{166}Dy doped SPIONs. The synthesis of radioactive ^{166}Dy-SPIONs was the same as the sysnthesis of non-radioactve Dy-SPIONs. The only differences were the extra safety measurements. Appendix A describes all the safety measurements that were taken to work in a laboratory with radioactive materials.

3.4.3. Determination of Dy-166 radiolabelling efficiency

$20\,\mu$L of 100 mM EDTA was added to the ^{166}Dy doped iron oxide nanoparticle. Then the samples were centrifuged at 21300 rcf for 30 min and washed with $20\,\mu$L of 100 mM EDTA and $750\,\mu$L MilliQ. The supernatent was stored in another Eppendorf tube. After washing 3 times $20\,\mu$L DTPA was added to the solution. These samples were stored at $37\,^{\circ}$C in a water bath. The counts per minute (CPM) of the nanoparticles and filtrates of all samples were measured with the gamma counter. ^{166}Dy was measured using its γ emission at 340 keV to 360 keV [5]. The radiolabelling efficiency of ^{166}Dy was calculated by the following formula:

$$radiolabelling\ efficiency\ [\%] = \frac{CPM(NPs)}{CPM(NPs) + \sum CPM(filtrate)} * 100\% \tag{3.2}$$

3.4.4. Determination of Ho-166 and Dy-166 retention

To determine the stability of ^{166}Ho and ^{166}Dy in the Dy doped SPIONs the solutions with the Dy-SPIONs were incubated at $37\,^{\circ}$C for 96 h. At different time point the samples were collected and washed by MilliQ water and $20\,\mu$L of 100 mM EDTA and then centrifuged again at 21300 rcf for 30 min. A mixture of ^{166}Ho and ^{166}Dy was measured from 81 keV to 82 keV and ^{166}Dy was measured from 340 keV to 360 keV. The CPM of the nanoparticles and the filtrate were measured to calculate the retention of ^{166}Dy with the next formula:

$$retention\ [\%] = \frac{CPM(NPs)}{CPM(NPs) + CPM(wash)} * 100\% \tag{3.3}$$

4

Results and Discussion

This chapter will show the results from the experiments explained in chapter 3. Relevant data from the non-radioactive and radioactive experiments is presented in this chapter followed by a discussion.

4.1. Non-radioactive experiments

The first research question was: *What is the influence of incorporating Dy in iron oxide nanoparticles on the size and what is the labelling efficiency of Dy in the iron oxide nanoparticles?* The results of the DLS and TEM will provide the size of the SPIONs and the results of the ICP/OES will show the labeling efficiency. As shown in section 3.3.3 the dispersion of the SPIONs was tried to be improved, the DLS will also show these results.

4.1.1. DLS

DLS was used to determine the hydrodynamic radius of the SPIONs. As explained in the section 2.1.3 the size of the NPs is important for in vivo applications, because if the NPs have a diameter smaller than 5.5 nm, the Dy-SPIONs can pass through the kidney pores and be cleared from the body by the renal system [19]. To find out if particles are indeed smaller than 5.5 nm, DLS was used. The graphs from the DLS show the hydrodynamic radius versus, the radius including the layer of PEG, versus the normalized intensity.

The synthesized iron oxide nanoparticles are superparamagnetic [15]. This means that using a magnetic stirrer could influence the electron spin and thus the synthesis of the SPIONs. To see if a magnetic stirrer did indeed affect the spin, SPIONs were synthesized using an magnetic and mechanic stirrer to examine the difference. In figure 4.1 are the results presented of this experiment. It is clear that there is more than one particle size, the peaks differ from several nanometers to thousands of nanometers. This indicates that the samples are polydisperse and that the SPIONs are aggregating or that there are impurities in the samples. The paper from Yin et al. from 2019 from which the synthesis method was adapted showed a hydrodynamic diameter of 5.3 nm, so the SPIONs were not aggregating there [17]. It is unclear what caused to aggregation to happen during the synthesis in this research. Another observation was the intensity increasing around the 0.1 nm. This is artefact that often occurs when using DLS and can therefore be ignored.

Figure 4.1 also shows that the aggregation happens with both the mechanic and the magnetic stirrer.The sizes are similar thus the magnetic stirrer did not influence the synthesis of the SPIONs. Due to these results the magnetic stirrer was used by synthesizing the next batches with the Dy doped SPIONs because it is easier to use.

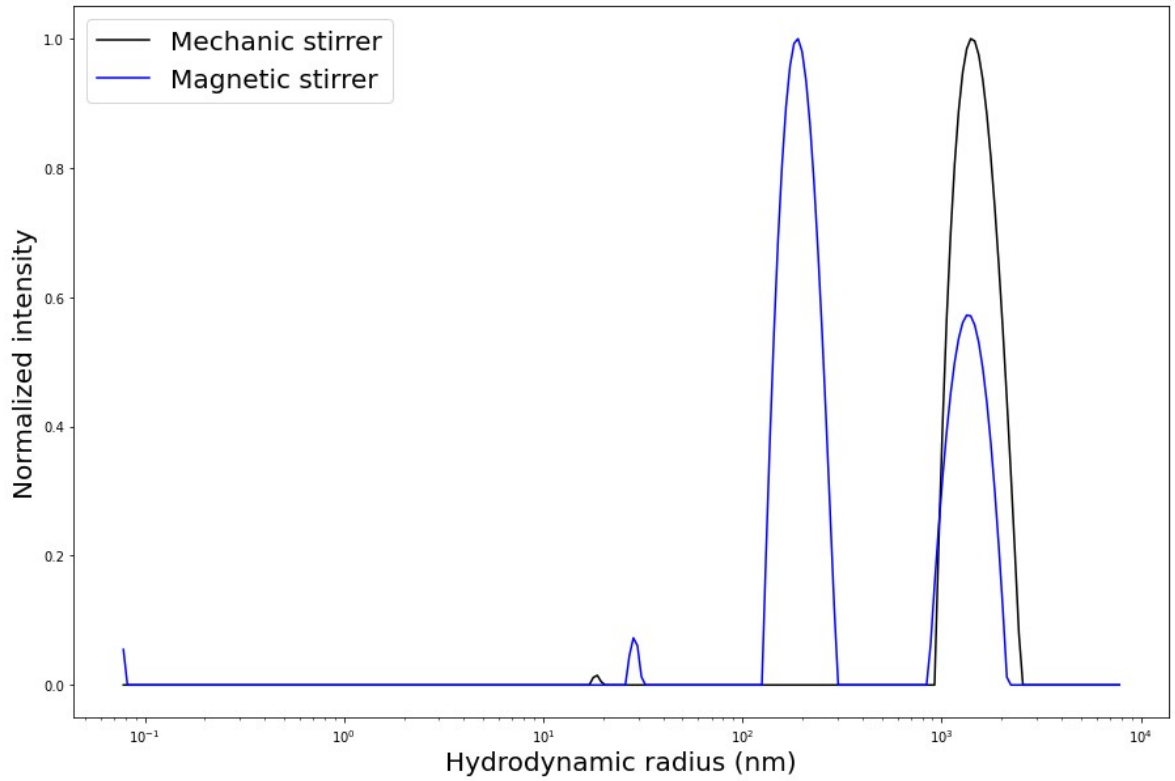

Figure 4.1: Hydrodynamic radius of SPIONs made with a mechanic and with a magnetic stirrer. The iron concentration of the SPIONs is [Fe^{3+}] = $50 * 10^3$ ppm.

The hydrodynamic radius of Dy doped SPIONs was compared to the SPIONs without dysprosium incorporated. Section 2.1.3 stated that the SPIONs have the unit cell $(Fe^{3+})_{24}[\square_8\, Fe_{403}{}^{3+}]\, O_{96}$ where the square $\square$ shows the empty spaces. During the synthesises the Dy should occupy these spaces. The size of the SPIONs with and without Dy should stay the same because the Dy will be inside in the vacancies of the nano particles [17]. Figure 4.2 shows samples of SPIONs with and without Dy in it.

The figure shows different peaks, the peaks on the right show the aggregated particles again. The small peaks on the left show the actual sizes of the SPIONs. The SPION without Dy had a hydrodynamic radius of 4.8 nm, so a diameter of 9.6 nm. The Dy doped SPION had a hydrodynamic radius of 6.9 nm, so a diameter of 13.8 nm. Part of the first research question is answered with this result: The influence of incorporating Dy in iron oxide nanoparticles on the diameter is that the Dy doped SPIONs are about 4 nm bigger than the SPIONs without Dy. The SPIONs with and without Dy both have a diameter larger than 5.5 nm and can thus not be cleared from by the renal system [19].

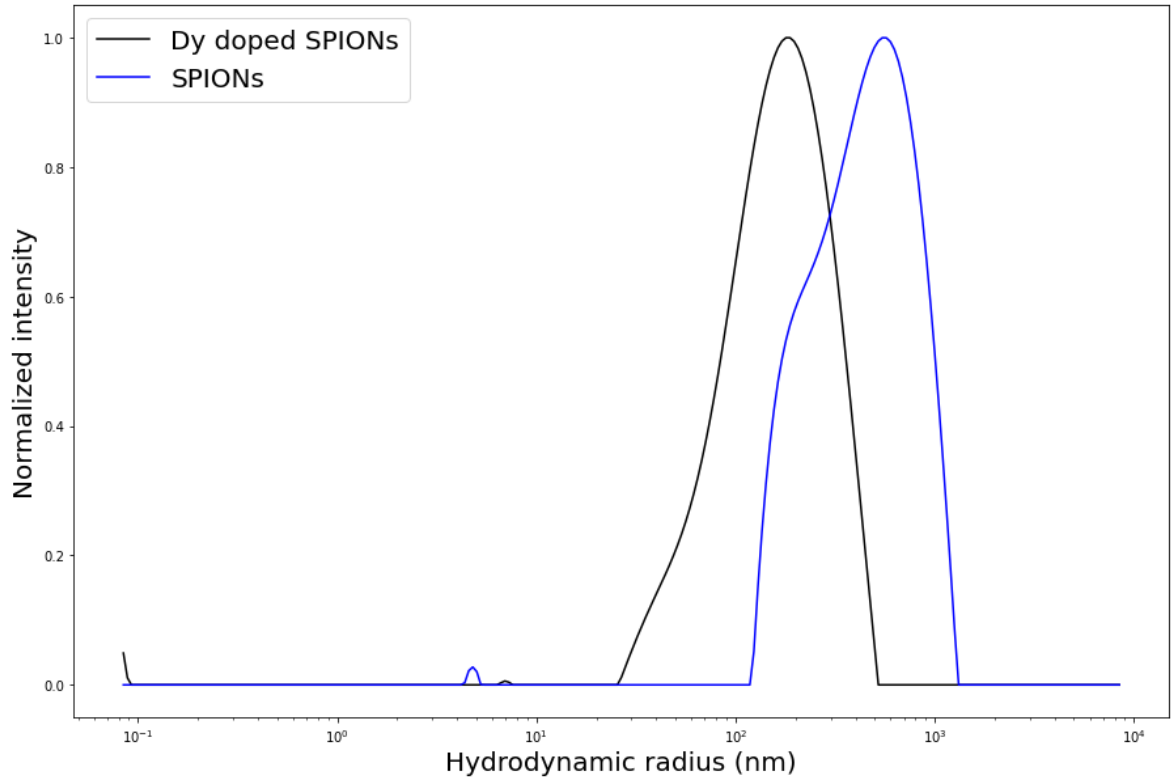

Figure 4.2: Hydrodynamic radius distribution of SPIONs with and without Dy incorporated, both with $[Fe^{3+}] = 50 * 10^3$ ppm.

The larger particles in figure 4.1 and 4.2 could be due to aggregation of the Dy-SPIONs. The method to prevent aggregation of the Dy-SPIONs was using the steric hindrance between SPIONs covered by PEG-bis(carboxymethyl)ether, MW = 138.12 kDa [34]. One of the carboxymethylether endings of this PEG binds to the SPION and the other ending can leads to electrostatic and steric repulsion which prevents aggregation. The $^{-}$COO endings can also form hydrogen- bonds with the surrounding water molecules and improve dispersion even more [35]. Even tough the SPIONs were coated with PEG, the SPIONs were still aggregating. The problem could have been that the molecular weight of the PEG was not high enough or that there was not enough PEG to surround all SPIONs. The MW of PEG chains is proportional to the polymer chain length. Therefore the MW is considered to be an important factor for effective surface shielding. Thus increasing the MW of PEG could prevent aggregation [36].

To reduce aggregation, a PEG with a higher MW was used: DSPE-PEG(2000) Carboxylic Acid, MW = 2780.38 kDa [37]. 1 mL of $10 * 10^3$ ppm DSPE-PEG(2000) Carboxylic Acid, was added to the solution with SPIONs. Figure 4.3 shows that the hydrodynamic radius of the SPIONs coated with DSPE-PEG(2000) Carboxylic are similar to the hydrodynamic radius of the SPIONs coated with PEG-bis(carboxymethyl)ether. So coating the SPIONs with a larger molecular weight did not change the dispersion.

It is also possible that not enough PEG was available to surround the SPIONs, thus the amount of PEG was doubled. 2 mL of $10 * 10^3$ ppm PEG-bis(carboxymethyl)ether, was added to the solution with SPIONs. The line with double the amount of PEG has an increased peak at 23 nm, so it could mean that the particles are aggregating less, but this still does not correspond to the expected size of one Dy-SPION.

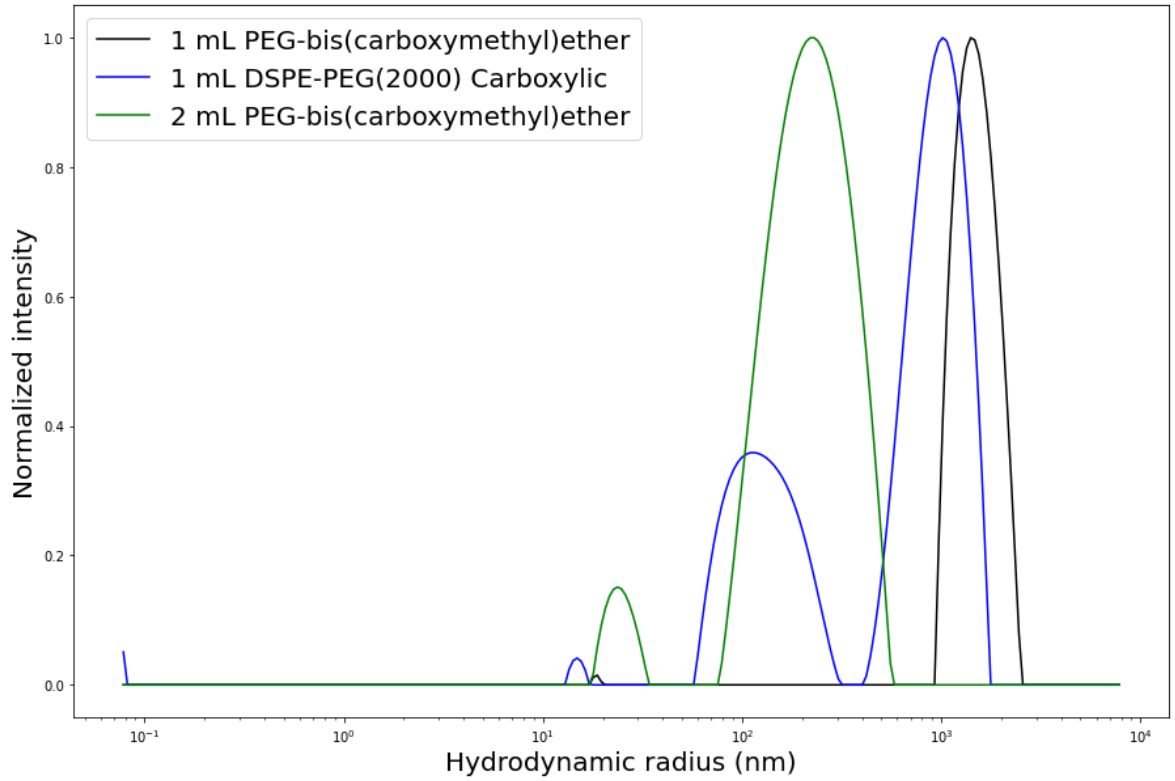

Figure 4.3: Hydrodynamic radius of SPIONs with 1 mL and 2 mL PEG-bis(carboxymethyl)ether, with a concentration of $10 * 10^3$ ppm and 1 mL of DSPE-PEG(2000) Carboxylic Acid, with a concentration of $10 * 10^3$ ppm .

Another method to improve the dispersion of the Dy-SPIONs was changing the pH of the solutions. Different concentrations of NaOH or HCl were prepared to make the base and acid solutions for the SPIONs. A higher pH and a lower pH could both improve the dispersion of the Dy-SPIONs.

Changes in surface charge can affect the disperion of the SPIONs. pH can influence the surface charge of the SPIONs. In the paper of Demangeat et al. from 1018 it was found that a pH further from the iso-electric point the maghemite NPs aggregate less [38]. The iso-electric point of iron oxide in water is at pH 8.6 [39]. The regular pH, which was used by all other experiments was tested with pH indicator papers to pH = 5.5. Therefore experiments were done with pH = 4 and 5, the results are shown in figure 4.4. A pH lower than 4 will not be feasible because the SPIONs will be damaged. The regular pH has one a large peak at 1400 nm. In a solution with pH = 5 there are particles with a hydrodynamic radius of 49 nm. There are still aggregated particles with a higher hydrodynamic radius of 530 nm, but these aggregated particles have a smaller hydrodynamic radius than at the regular pH. pH = 4 has a small peak at 52 and the broad peak of aggregated particles shifts even more to the left to 350 nm. So even though no small SPIONs were found at the particle size that was expected, the SPIONs started to aggregate less at lower pHs.

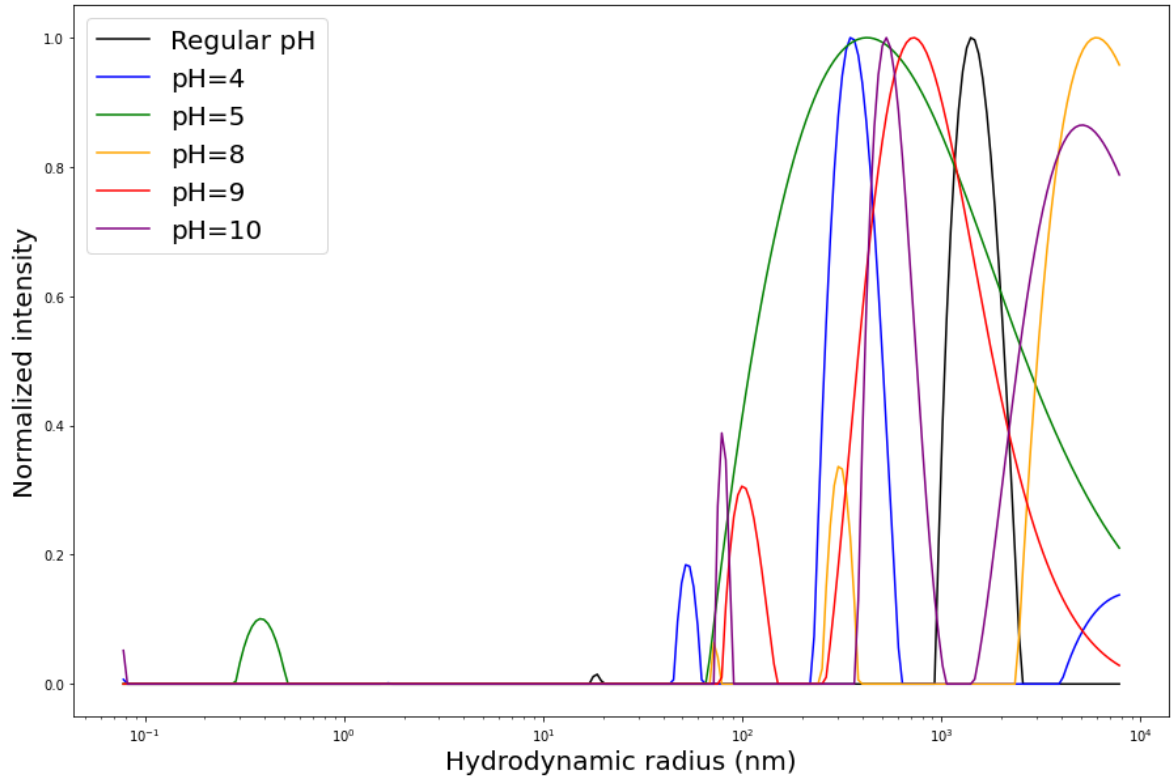

Figure 4.4: Hydrodynamic radius distribution of Dy-SPIONs, with [Fe^{3+}] = $50 * 10^3$ ppm, dissolved in solutions with pH = 4, 5, 8, 9 and 10.

PEG-bis(carboxymethyl)ether has $^-$COOH ending. Above the iso-electric point, at pH = 9 and pH = 10, these $^-$COOH endings will be protonated. The protenated endings will then form hydrogen bonds with water, and then are the NPs more hydrophilic. The results of the DLS with pH = $8, 9, 10$ are shown in figure 4.4. At pH = 8 are very large particles. pH 8 is very close to the iso-electric point, so a lot of aggregation occurs. At pH = 8 are also a some smaller particles with a hydrodynamic radius of 300 nm. The green line of pH = 9 shows a broad peak similar to pH =8, but also shows less aggregated particles with a hydrodynamic radius of 100 nm. At pH = 10 the hydrodynamic radius was 79 nm. So the particles are aggregating less when further away from the iso-electric point. There are still no particles found with the size of non-aggregated SPIONs, but less aggregation is achieved. A lower pH resulted in less aggregation than a high pH.

The fourth method to improve the dispersion of the Dy-SPIONs was by sonicating before adding the PEG. Sonication is a process in which sound waves are used to agitate particles in a medium, this could improve the stability of Dy-SPIONs [40]. This was combined with scaling down the synthesis. Two solutions with SPIONs were prepared with [Fe^{3+}] = $10 * 10^3$ ppm. With the lower concentration less SPIONs were synthesized, and thus less aggregation was possible.

One of these solution was sonicated at at $40\,^{\circ}$C for 60 min and the other solution was sonicated for 90 min. After the sonication 1 mL PEG was added and the solution was heated again at $60\,^{\circ}$C in silicon oil. After this the solution was cooled down to room temperature. The DLS results are shown in figure 4.5. The black line shows the SPIONs which were not sonicated and/or scaled-down. The blue and green line show the sonicated SPIONs with lowered concentration. The blue and green line are very similar and both have particles with a hydrodynamic radius of 300 nm. This shows that sonicating for 60 or 90 minutes does not change the dispersion. The regular sample which had particles with hydrodynamic radius of 460 nm. This shows that the combination of sonicating and lowering the concentration had a small effect on the dispersion.

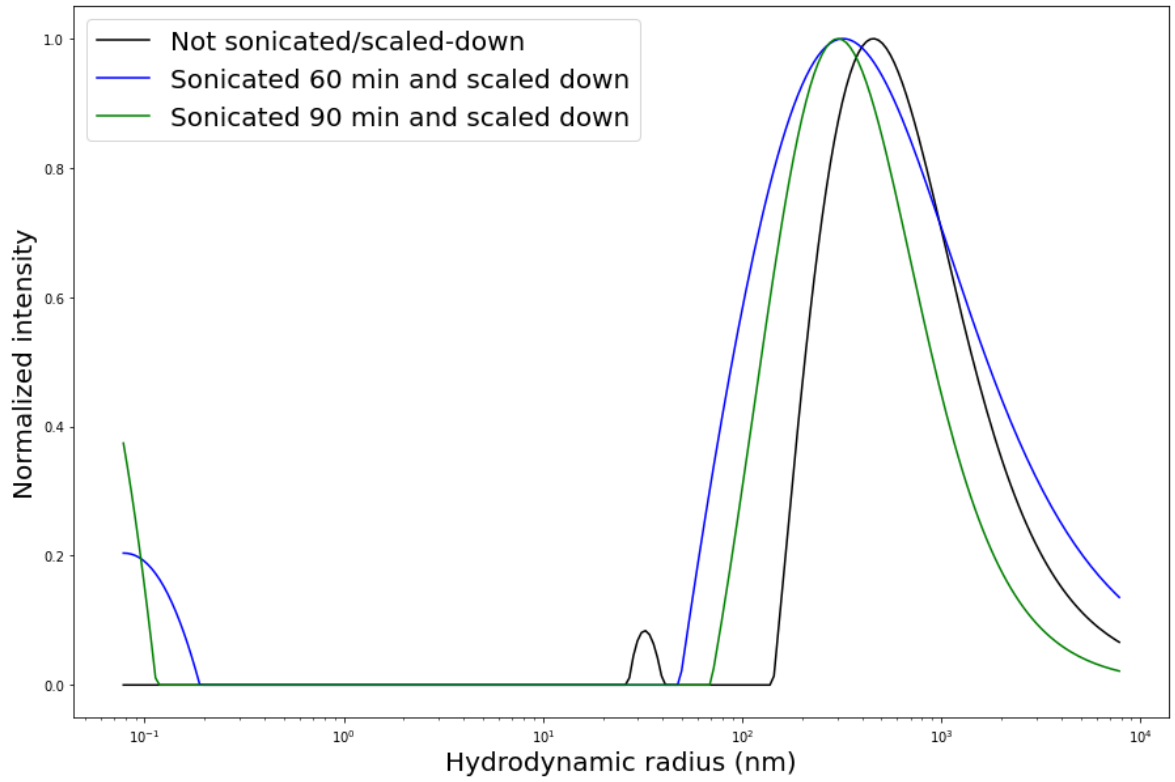

Figure 4.5: Hydrodynamic radius distribution of Dy-SPIONs, with [Fe^{3+}] = $10 * 10^3$ ppm, after sonicating and scaling down the synthesis. The SPIONs which were not scaled-down have a iron concentration of $50 * 10^3$ ppm.

The solutions with SPIONs were filtered with a syringe filter. The goal of this filter was to make sure that any aggregated molecules or impurities would be filtered out and only well dispersed SPIONs stayed in the solution. The samples were filtered using a $0.22\,\mu$m syringe filter, see figure 4.6 for the DLS results. After filtering there are SPIONs with a hydrodynamic radius of 5.9 nm. This size indicates non-aggregated SPIONs. This means that the synthesis of the SPIONs with the right size was successful, but that they would not disperse. There is also a peak which shows that there are still aggregated particles with a hydrodynamic radius of 100 nm and larger. So directly after filtering the aggregated particles and impurities are partly filtered out. After 7 days the samples were measured again to see if they would stay separated, but this was not the case. In figure 4.6 is shown by the green line that the peak at 5.9 nm decreases again and thus the SPIONs aggregated again.

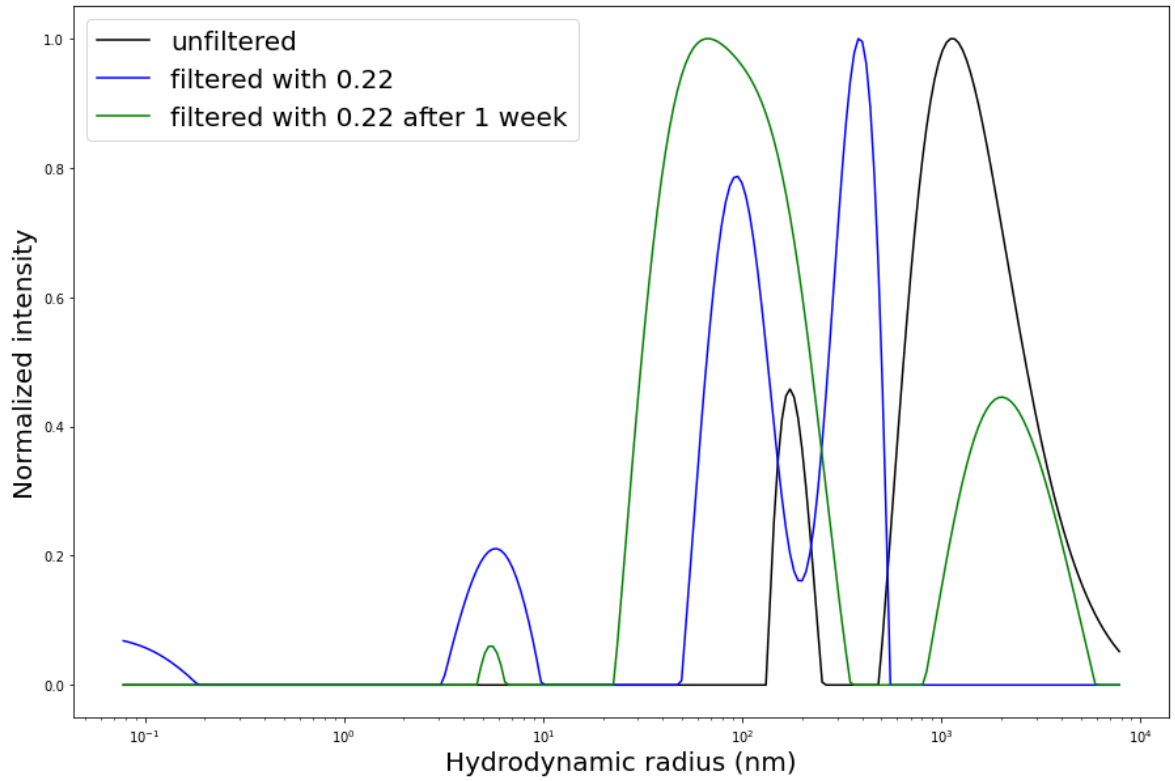

Figure 4.6: Hydrodynamic radius distribution of Dy-SPIONs, with [Fe^{3+}] = $50 * 10^3$ ppm, after filtering the solution.

4.1.2. TEM

From the results of the DLS the hydrodynamic radius of the SPIONs was found. To find the actual size of the SPIONs TEM was used. TEM shows the particles at the nano-scale due to high magnification. Figure 4.7 is an image of a solution with Dy doped SPIONs. The Dy-SPIONs are indicated by black dots. The figure shows that the SPIONs are aggregated. This means that the data of the TEM supports the data of the DLS. An important observation is the crystals present in the samples. NaOH was used to synthesize the SPIONs and this shows that not all NaOH has reacted and that it is still present in the samples. This means that the big peaks of the DLS results can also be due to impurities and are not only because of aggregated nano particles.

The Dy-SPIONs in the image were counted and the diameters were determined using ImageJ software. ImageJ processes and analyses scientific images such as TEM images, by detecting and measuring dots. The program gives a mean diameter and a standard deviation of the Dy doped SPION so a histogram of the sizes of the SPIONs was made using python, see figure 4.8. The Dy-SPIONs differ in size. The average size of the Dy doped SPIONs measured from this image is 6.1 ± 1.5 nm. This corresponds to the size found in literature of a γ-Fe_2O_3 nanoparticle synthesized by Demangeat et al. in 2018 [38]. It is possible that the larger SPIONs shown in the histogram are already 2 SPIONs aggregated together, and the average size of the particle is slightly lower, but the TEM image is not clear enough to be certain of this.

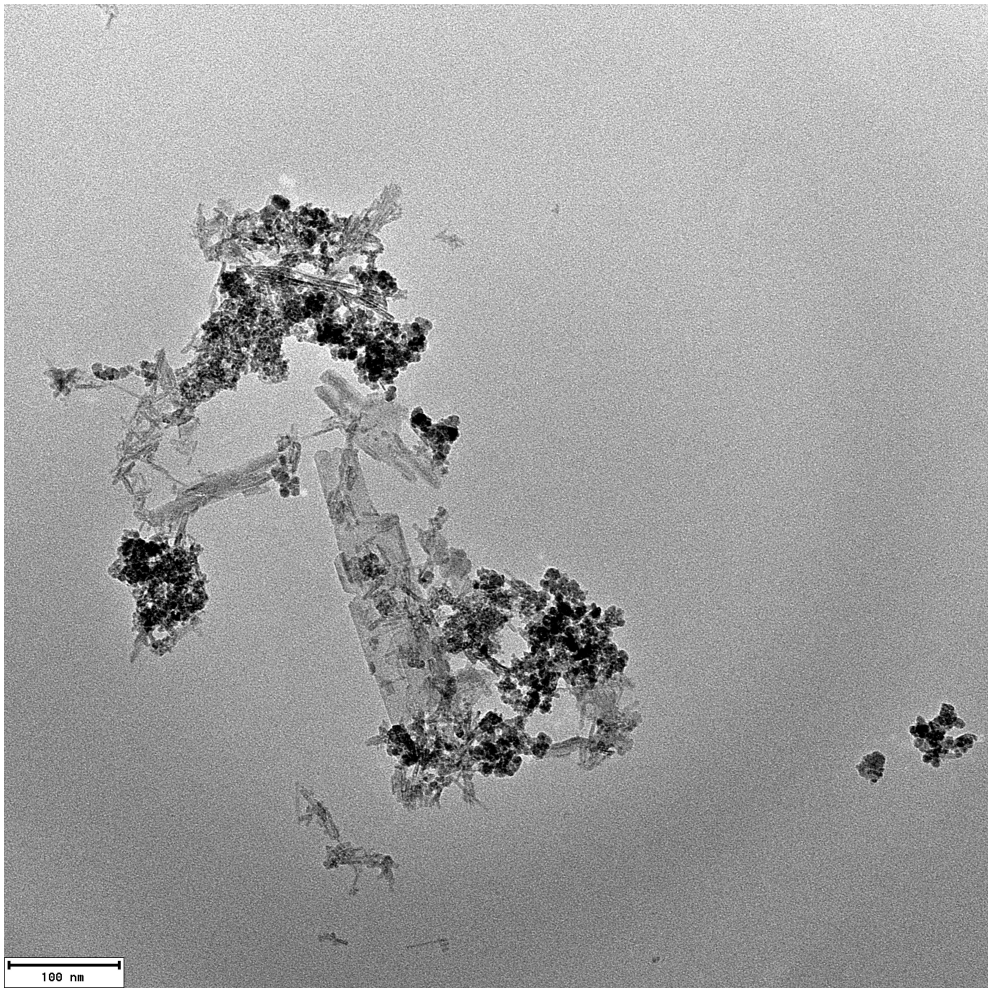

Figure 4.7: A TEM image of Dy-SPIONs, with [Fe^{3+}] = $50 * 10^3$ ppm. The black dots indicate SPIONs and the crystals are unreacted NaOH.

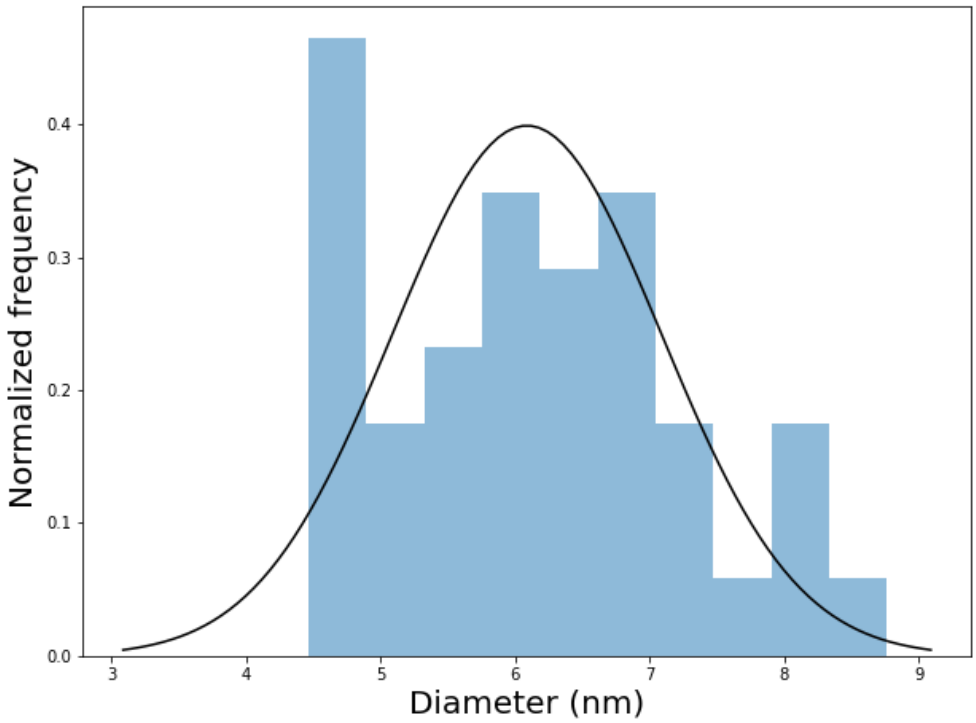

Figure 4.8: A histogram of the sizes of the SPIONs, with [Fe^{3+}] = $50 * 10^3$ ppm, extracted from the TEM image.

4.1.3. ICP/OES

ICP/OES was used to find the labelling efficiency of the Dy in the Dy-SPIONs. The ICP/OES determined the concentration of Dy and Fe in each sample. The presence of Dy was measured at a wavelength of 353.170 nm, 364.540 nm and 394.468 nm. The presence of Fe was measured at 238.204 nm, 239.562 nm and 259.939 nm. The concentrations of these wavelengths were averaged and the concentration in mg/L found by the ICP is shown in table 4.1.

With the ICP/OES results labelling efficiency was calculated, see table 4.1. The labeling efficiency represents how much Dy is retained in the Dy-SPIONs. How much Dy was added during the synthesis and the molecular weight of Dy are known and thus the concentration was calculated. With both concentrations known the labelling efficiency was calculated with equation 3.1. $[Dy_{ICP/OES}]$ was the concentration of dysprosium left in the sample after washing 3 times with milliQ and $[Dy_{synthesis}]$ was the amount of Dy added during the synthesises. Table 4.1 shows the calculations and the labelling efficiencies are displayed in figure 4.9. It shows that the labelling efficiencies are very low with an average of 3.21 ± 0.8%. Thus much more Dy is added than what is actually found in the SPIONs by the ICP/OES.

The low labelling efficiency of Dy in the Dy-SPIONs can be explained when looking at the yield of SPIONs which is also shown in table 4.1. The average yield of the SPIONs is 10.02 ± 1.6 %. So not all the iron is used to make the SPIONs and almost 90 % of the iron is washed away. The supernatant of the SPIONs before washing was orange, the color of Fe^{3+}, which indicates the iron was indeed in the supernatant and not all incorporated into the SPIONs. The SPIONs were synthesized using the co-precipitation technique. The co-precipitation technique involves the precipitation of a salt precursor with the help of a base in a solvent [41]. The co-precipitation mechanism has to steps, first the formation of iron hydroxide particles, ferrihydrite, then the formation of the SPIONs. The ferrihydrite formed within seconds, this was visible as the reaction solution turned from yellow to dark brown within seconds. Then the γ-Fe_2O_3 formed, this could have taken a few minutes [42]. During these minutes it is possible that the ferrihydrite already started to aggregate before the SPIONs formed, which could have lowered the yield of the SPIONs [43].

Table 4.1: Table of the concentration used to calculate the labelling efficiencies, the labelling efficiencies of Dy in the Dy-SPIONs and the yield of the SPIONs.

Batch	$[Dy_{ICP/OES}]$ [mmol/L]	$[Dy_{synthesis}]$ [mmol/L]	**Labelling efficiency Dy** [%]	**Yield of SPIONs** [%]
1.1	0.297	2.46	2.65 ± 0.35	9.72 ± 0.27
1.2	0.345	2.46	3.08 ± 0.09	10.46 ± 0.34
2.1	0.243	2.46	2.17 ± 0.17	7.09 ± 0.21
2.2	0.369	2.46	3.30 ± 0.12	11.22 ± 0.24
3.1	0.362	2.46	3.23 ± 0.26	9.36 ± 0.27
3.2	0.541	2.46	4.83 ± 0.69	12.28 ± 0.24

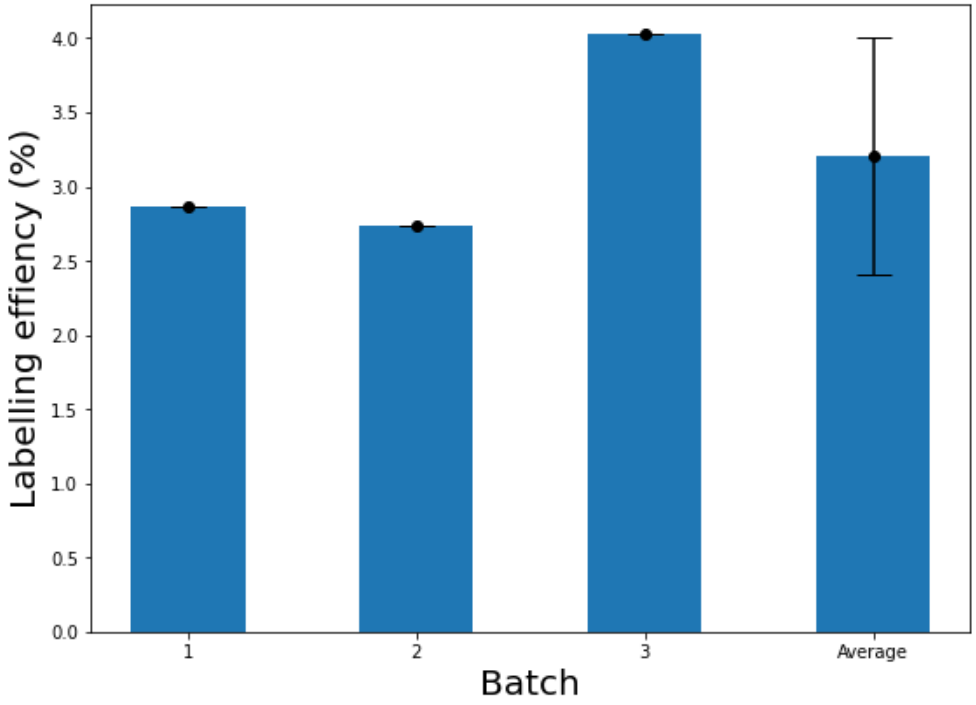

Figure 4.9: The bars represent the averages of the labelling efficiencies of the two samples per batch. It represents how much dysprosium was incorporated into the Dy-SPIONs, with [Fe^{3+}] = $50 * 10^5$ ppm. The last bar shows the average of the labelling efficiencies and the error bar represents the standard deviations of three independent experiments.

4.2. Radioactive experiments

The research question for the radioactive part was: *What is the retention of the daughter nuclide of ^{166}Dy (^{166}Ho) on the ^{166}Dy doped iron oxide nanoparticle carrier?* In this section the results from each radioactive experiment will be explained and the research question will be answered.

First, the measurements of the radiolabelling efficiency of the ^{166}Dy were performed. Then the samples were measured again after 24, 48, 72 and 96 hours to determine the retention of ^{166}Dy and ^{166}Ho. As written in section 2.1.2 ^{166}Dy has β^- and γ decay. γ decay is easier to detect and therefore only γ decay was detected during these experiments.

4.2.1. Radiolabelling efficiency of Dy-166

The synthesis of the ^{166}Dy-SPIONs was almost the same as for the Dy-SPIONs. The Dy source was a mixture of non-radioactive $Dy(NO_3)_3 \cdot 5\,H_2O$ and radioactive $^{166}Dy(NO_3)_3 \cdot 5\,H_2O$. Due to the decay of ^{166}Dy, ^{166}Ho was also present in the stock solution, which was considered negligible during the synthesis. Two samples of three independently synthesized solutions of ^{166}Dy doped SPIONs were washed with EDTA and MiliQ to remove all unbounded ^{166}Dy. The radiolabelling efficiencies were calculated per sample by comparing the counts per minute of the NPs and the washed solutions with the Wallac Wizard2 2480. The gamma emission of ^{166}Dy was measured from 340 keV to 360 keV for 5 minutes. The energy that was measured corresponds to the energy of a γ ray when ^{166}Dy decays to ^{166}Ho. The CPM correspond to the activity which is a trace for the amount ^{166}Dy incorporated in the SPIONs. In table 4.2 and figure 4.10 are the radiolabelling efficiencies shown. Batch 3 was made 4 days later than batch 1 and 2 and thus the activity of batch 3 was lower during the measurements. The radiolabbeling efficiency of the first sample of batch 1 is significantly higher than the others, the reason for this is unclear since the same conditions were used for synthesis and measurements for all samples.

Table 4.2: Radiolabelling of ^{166}Dy in the ^{166}Dy-SPIONs.

Batch	**Radiolabelling efficiency** [%]
1.1	9.09
1.2	3.30
2.1	3.12
2.2	1.26
3.1	0.82
3.2	1.14

The average labelling efficiency measured with ICP was 3.21 ± 0.8 % and the radiolabelling measured with the Wallac Wizard2 2480 was 3.12 ± 2.2 %. So the ICP/OES and Gamma counter have similar outcome.

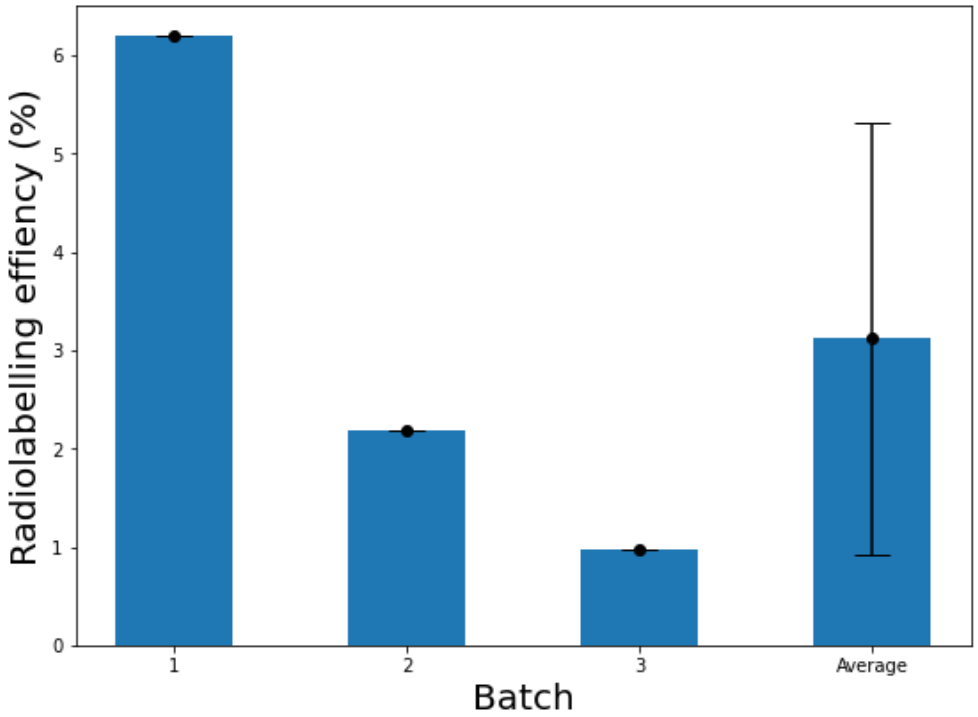

Figure 4.10: The bars represent the averages of the labelling efficiencies of the two samples per batch. It represents how much ^{166}Dy was incorporated into the ^{166}Dy-SPIONs, with [Fe^{3+}] = $50 * 10^5$ ppm. The last bar shows the average of all labelling efficiencies and the error bar represents the standard deviations of three independent experiments.

4.2.2. Retention of Dy-166 and Ho-166

As mentioned in section 1.1 the goal of this thesis was to develop a nanoparticle based carrier for ^{166}Dy/^{166}Ho generator which will prevent the loss of the daughter nuclide ^{166}Ho induced by internal conversion. Preventing the loss of the mother and daughter nuclide will prevent damage to healthy tissue. To see if the iron oxide nano particles would be successful for this, the retention of ^{166}Dy and ^{166}Ho was measured.

To measure the retention of the internally converted of ^{166}Dy to ^{166}Ho, the ^{166}Dy-SPIONs were incubated in MiliQ water with $20\,\mu$L of 100 mM DTPA at $37\,^{\circ}$C for 96 h. Every 24 h, the samples were centrifuged to separate the SPIONs from free $^{166}Dy^{3+}$ and $^{166}Ho^{3+}$. The counts per minutes were measured in two windows: $65 - 90$ keV and $340 - 460$ keV. The first window is a mixture of ^{166}Dy and ^{166}Ho and the second window is only ^{166}Dy. These windows were combined for the calculations of the retention. The retention was calculated with formula 3.3 and the results of the calculations are shown in table 4.3. The averages of the results are shown in figure 4.11. The table also shows that batch 1 and 2 it were not washed and measured at 48 h and 72 h, because it was weekend and there was no access to the lab. At 96 h the activity of batch 3 was too low and these results could not be used either, because of this an error bar is only shown at 24 h in figure 4.11. The figure does show a clear trend line with a small decrease in retention every 24 hours, which indicates that the results are accurate.

Table 4.3: Retention of ^{166}Dy + ^{166}Ho in the SPIONs displayed in % at different time points when kept in a water bath at $37\,^{\circ}$C.

Batch	24 h	48 h	72 h	96 h
1.1	83.36	-	-	78.53
1.2	84.59	-	-	77.80
2.1	88.44	-	-	81.86
2.2	85.88	-	-	78.45
3.1	88.56	80.82	78.66	-
3.2	96.86	91.38	85.70	-

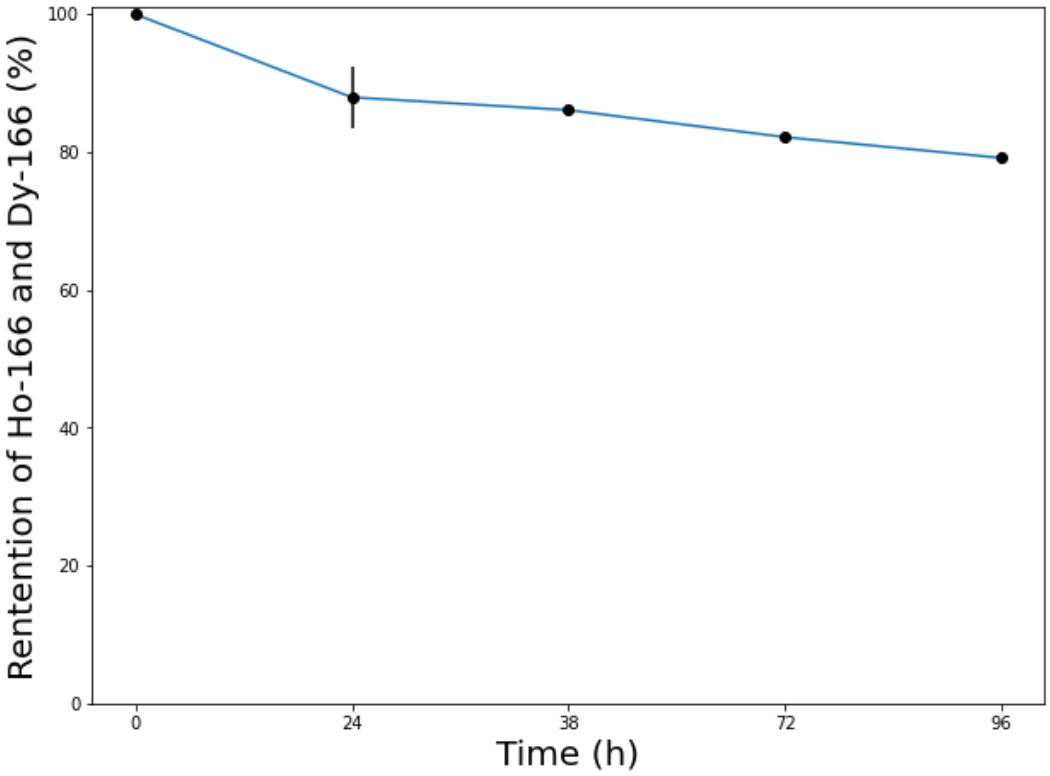

Figure 4.11: The retention of ^{166}Dy + ^{166}Ho in the SPIONs, with [Fe^{3+}] = $50 * 10^5$ ppm, displayed in %. The error bar at 24 h, represents the standard deviations of three independent experiments.

The retention of ^{166}Dy + ^{166}Ho is 79.2 ± 1.8 % after 96 h, this is much higher than the retention of 28% by conventional chelators [5]. This means that the SPIONs are safer carriers for the ^{166}Dy/^{166}Ho in vivo generator than the conventional chelator DOTA. Still about 20 % of the ^{166}Dy + ^{166}Ho is released so there is room for improvement. In section 2.1.3 is explained how the maghmite supercell looks and that there are vacancies in the supercell. The ^{166}Dy and thus also the ^{166}Ho fill the vacancies during the synthesis. It is possible that not all vacancies were filled during the synthesis and that when the SPIONs were washed the DPTA could fill the vacancies. This is a possible reason for the ^{166}Dy and ^{166}Ho getting out.

5

Conclusions and Recommendations

5.1. Conclusion

The first research question was: *What is the influence of incorporating Dy in iron oxide nanoparticles on the size and what is the labelling efficiency of Dy in the iron oxide nanoparticles?* The DLS results showed that the SPIONs without Dy had a diameter of 9.6 nm, and the SPIONs with Dy incorporated had a diameter of 13.8 nm. Thus the influence of incorporating Dy in SPIONs is that the Dy doped SPIONs are about 4 nm bigger than the SPIONs without Dy. The DLS also showed peaks from hundreds to thousands nanometers. Together with the TEM images it was concluded that these peaks indicate aggregated SPIONs and impurities. Filtering the Dy doped SPIONs with a 0.22 µm syringe filter resulted in a bigger peak at 5.9 nm than without filtering. So the larger particles were removed during the filtering which made the non-aggregated SPIONs visible by the DLS. After 7 days the SPIONs were aggregating again. There was no method found to keep the SPIONs from aggregating for a longer period. The TEM images showed that the average diameter of the Dy-SPIONs is 6.1 ± 1.5 nm. The labelling efficiency measured with ICP/OES was 3.21 ± 0.8 % and the radiolabelling effiency measured with the Wallac Wizard2 2480 was 3.12 ± 2.2 %.

The research question for the radioactive part was: *What is the retention of the daughter nuclide of ^{166}Dy (^{166}Ho) on the ^{166}Dy doped iron oxide nanoparticle carrier?* The retention of ^{166}Dy $+$ ^{166}Ho is 79.2 ± 1.8 % after 96 h, this is much higher than the retention of 28% by conventional chelators [5]. This means that the SPIONs are safer carriers for the ^{166}Dy/^{166}Ho in vivo generator than the conventional chelators.

5.2. Recommendations

The results of the retention of ^{166}Dy and ^{166}Ho showed that SPIONs can potentially be used as a carrier of the radionuclide, but more research is needed to be sure. Further research is needed on the following aspects:

1. Synthesizing SPIONs which will not aggregate by adding another layer on top of the SPIONs made from hydrolized tetraethylorthosilicate (TEOS) [35].
2. Synthesizing SPIONs in a non-aqueous phase to prevent aggregating [41].
3. Synthesizing SPIONs with a maximum size of 5.5 nm by using calcination [44].
4. Optimizing the (radio)labelling efficiency of Dy in SPIONs by varying the concentration and volumes of Dysprosium.
5. Improving the retention of ^{166}Dy $+$ ^{166}Ho by using a material with a high atomic number as NPs [45].

To keep the SPIONs from aggregating it is possible to add another layer on top of the SPIONs made from silica. Hydrolized tetraethylorthosilicate could be this silica source. Coating the SPIONs with this hydrolized TEOS, together with sonicating, could decrease the aggregating of the SPIONs [35]. Another way to keep the SPIONs from aggregating would be to do the synthesis in a non-aqueous phase. The synthesis of iron oxide nanoparticles in organic solvents offers higher quality crystals in comparison to those obtained in an aqueous solvent [41]. Synthesizing the SPIONs in organic solvents might also improve the size of the nano particles so that the limit of 5.5 nm will not be reached. Another way to make small SPIONs might be possible with calcination. Calcination means heating a substance to a high temperature but below the melting or fusing point. This causes the material the loss of moisture, reduction or oxidation, and forces dissociation into simpler substances. Calcination is already tested on ZnO and this resulted in smaller crystalline size of the ZnO NPs when the calcination temperature was increased [44]. The same effect could occur when SPIONs are calcinated. After synthesizing small, well-dispersed SPIONs the (radio)labbelling needs to be improved. Looking into varying the concentration or volumes of the Dysprosium source could increase the (radio)labelling efficiency. To improve the retention a material with a high atomic number could be used as NPs [45]. With a high atomic number more free electrons are available. When the highly positive ^{166}Ho ion extracts electrons from its neighbouring atoms, electrons can be quickly redistributed to fill in the new vacancies and this could increase the retention.

References

[1] WHO. *Cancer*. 2022. URL: https://www.who.int/news-room/fact-sheets/detail/cancer (visited on 10/11/2022).

[2] S. E. Pool, E. P. Krenning, G. A. Koning, C. H.J. van Eijck, J. J.M. Teunissen, B. Kam, R. Valkema, D. J. Kwekkeboom, and M. de Jong. "Preclinical and Clinical Studies of Peptide Receptor Radionuclide Therapy". In: *Seminars in Nuclear Medicine* 40.3 (2010). Antibodies and Peptides in Nuclear Medicine Imaging and Therapy, pp. 209–218. ISSN: 0001-2998. DOI: https://doi.org/10.1053/j.semnuclmed.2009.12.001. URL: https://www.sciencedirect.com/science/article/pii/S0001299809001147.

[3] G. Sgouros, L. Bodei, M. R. McDevitt, and J. R. Nedrow. "Radiopharmaceutical therapy in cancer: clinical advances and challenges". In: *Nature Reviews Drug Discovery* 19 (9 2020), pp. 589–608. DOI: https://doi.org/10.1038/s41573-020-0073-9. URL: https://www.nature.com/articles/s41573-020-0073-9#citeas.

[4] S. Shen, D. Jiang, L. Cheng, Y. Chao, K. Nie, Z. Dong, C. J. Kutyreff, J. W. Engle, P. Huangand W. Cai, and Z. Liu. "Renal-Clearable Ultrasmall Coordination Polymer Nanodots for Chelator-Free 64Cu-Labeling and Imaging-Guided Enhanced Radiotherapy of Cancer". In: *ACS Nano* 11.9 (2017). PMID: 28853861, pp. 9103–9111. DOI: 10.1021/acsnano.7b03857. eprint: https://doi.org/10.1021/acsnano.7b03857. URL: https://doi.org/10.1021/acsnano.7b03857.

[5] R. Wang, B. Ponsard, H. Wolterbeek, and A. Denkova. "Core–shell structured gold nanoparticles as carrier for 166Dy/166Ho in vivo generator". In: *EJNMMI Radiopharmacy and Chemistry* 7 (1 2020). DOI: https://doi.org/10.1186/s41181-022-00170-3. URL: https://ejnmmipharmchem.springeropen.com/articles/10.1186/s41181-022-00170-3.

[6] T. Karpov, A. Postovalova, D. Akhmetova, A. R. Muslimovand E. Eletskaya, M. V. Zyuzin, and A. S. Timin. "Universal Chelator-Free Radiolabeling of Organic and Inorganic-Based Nanocarriers with Diagnostic and Therapeutic Isotopes for Internal Radiotherapy". In: *Chemistry of Materials* 34.14 (2022), pp. 6593–6605. DOI: 10.1021/acs.chemmater.2c01507. eprint: https://doi.org/10.1021/acs.chemmater.2c01507. URL: https://doi.org/10.1021/acs.chemmater.2c01507.

[7] Institute of Medicine and National Research Council. *Advancing Nuclear Medicine Through Innovation*. Washington, DC: The National Academies Press, 2007. ISBN: 978-0-309-11067-9. DOI: 10.17226/11985. URL: https://nap.nationalacademies.org/catalog/11985/advancing-nuclear-medicine-through-innovation.

[8] N. Daems, C. Michiels, S. Lucas, S. Baatout, and A. Aerts. "Gold nanoparticles meet medical radionuclides". In: *Nuclear Medicine and Biology* 100-101 (June 2021). DOI: 10.1016/j.nucmedbio.2021.06.001.

[9] J. van den Eijnde and L. Roobol. *Practical Radiation Protection*. 4th ed. Syntax Media, 2018.

[10] B. Milborne, A. Arafat, R. Layfield, A. Thompson, and I. Ahmed. "The use of biomaterials in internal radiation therapy". In: *Recent Progress in Materials* 2.9 (2 2020), pp. 1–34. DOI: 10.21926/rpm.2002012. URL: https://www.lidsen.com/journals/rpm/rpm-02-02-012.

[11] P. E. Edem, J Fonslet, A. Kjær, M. Herth, and G. Severin. "In Vivo Radionuclide Generators for Diagnostics and Therapy". In: *Bioinorganic Chemistry and Applications* 2016 (2016), pp. 1–8.

[12] N. Klaassen, M. Arntz, G. Arranja, J. Roosen, and J. Nijsen. "The various therapeutic applications of the medical isotope holmium-166: a narrative review". In: *EJNMMI Radiopharmacy and Chemistry* 4.1 (2010). Antibodies and Peptides in Nuclear Medicine Imaging and Therapy, pp. 1–26. DOI: 10.1186/s41181-019-0066-3. URL: https://doi.org/10.1186/s41181-019-0066-3.

[13] J. R. Zeevaart, Z. Szücs, S. Takács, N. V. Jarvis, and D. Jansen. "Recoil and conversion electron considerations of the 166Dy/166Ho in vivo generator". In: 100.2 (2012), pp. 109–113. DOI: doi:10.1524/ract.2011.1841. URL: https://doi.org/10.1524/ract.2011.1841.

[14] The Editors of Encyclopaedia. *Britannica*. 2022. URL: https://www.britannica.com/science/iron-chemical-element (visited on 10/25/2022).

[15] S. Savliwala, A. Chiu-Lam, M. Unni, A. Rivera-Rodriguez, E. Fuller, K. Sen, M. Threadcraft, and C. Rinaldi. "Chapter 13 - Magnetic nanoparticles". In: *Nanoparticles for Biomedical Applications*. Ed. by E. Ji Chung, L. Leon, and C. Rinaldi. Micro and Nano Technologies. Elsevier, 2020, pp. 195–221. ISBN: 978-0-12-816662-8. DOI: https://doi.org/10.1016/B978-0-12-816662-8.00013-8. URL: https://www.sciencedirect.com/science/article/pii/B9780128166628000138.

[16] Y. Piñeiro, Z. Vargas, J. Rivas, and M. A. Lopez-Quintela. "Iron Oxide Based Nanoparticles for Magnetic Hyperthermia Strategies in Biological Applications". In: *European Journal of Inorganic Chemistry* 2015 (27 2015), pp. 4495–4509. DOI: https://doi.org/10.1002/ejic.201500598.

[17] J. Yin, F. Xu, H. Qu, C. Li, S. Liu, L. Liu, and Y. Shao. "Dysprosium-doped iron oxide nanoparticles boosting spin–spin relaxation: a computational and experimental study". In: *Phys. Chem. Chem. Phys.* 21 (22 2019), pp. 11883–11891. DOI: 10.1039/C9CP00463G. URL: http://dx.doi.org/10.1039/C9CP00463G.

[18] H.S. Choi, W. Liu, P. Misra abd E. Tanaka, J.P. Zimmer, B. Itty Ipe, M.G. Bawendi, and J.V. Frangioni. "Renal clearance of quantum dots". In: *Nat Biotechnol* 25 (2007), pp. 1165–1170. DOI: 10.1038/nbt1340.

[19] J. Liu, M. Yu, C. Zhou, and J. Zheng. "Renal clearable inorganic nanoparticles: a new frontier of bionanotechnology". In: *Materials Today* 16.12 (2013), pp. 477–486. ISSN: 1369-7021. DOI: https://doi.org/10.1016/j.mattod.2013.11.003. URL: https://www.sciencedirect.com/science/article/pii/S1369702113003878.

[20] N. V. S. Vallabani and S. Singh. "Recent advances and future prospects of iron oxide nanoparticles in biomedicine and diagnostics". In: *3 Biotech* 8.6 (June 2018), p. 279. ISSN: 2190-572X. DOI: 10.1007/s13205-018-1286-z. URL: https://europepmc.org/articles/PMC5984604.

[21] A. Ali, H. Zafar H, M. Zia, I. Ul Haq I, A. R. Phull, J. S. Ali JS, and A. Hussain. "Synthesis, characterization, applications, and challenges of iron oxide nanoparticles." In: *Nanotechnol Sci Appl.* 9 (2016), pp. 49–67. DOI: 10.2147/NSA.S99986.

[22] S. Goel, F. Chen, E. B. Ehlerding, and W. Cai. "Intrinsically Radiolabeled Nanoparticles:An Emerging Paradigm". In: *Small* 10 (19 2014), pp. 3825–3830. DOI: 10.1002/smll.201401048.

[23] F. Chen, K. Ma, L. Zhang, B. Madajewski andP. Zanzonico, S. Sequeira, M. Gonen, U. Wiesner, and Bradbury M. "Target-or-Clear Zirconium-89 Labeled Silica Nanoparticles for Enhanced Cancer-Directed Uptake in Melanoma: A Comparison of Radiolabeling Strategies". In: *Chemistry of Materials* 29.19 (2017), pp. 8269–8281. DOI: 10.1021/acs.chemmater.7b02567. eprint: https://doi.org/10.1021/acs.chemmater.7b02567. URL: https://doi.org/10.1021/acs.chemmater.7b02567.

[24] Z. Neale. *Inductively coupled plasma optical emission spectroscopy (ICP-OES) Overview*. 2020. URL: https://www.youtube.com/watch?v=InFhIHPZYIc (visited on 11/08/2022).

[25] S. Ghosh, V. L. Prasanna, B. Sowjanya, P. Srivani, M. Alagaraja, and D. Banji. "Inductively Coupled Plasma –Optical Emission Spectroscopy: A Review." In: *Asian Journal of Pharmaceutics* 3.1 (2013), pp. 24–33.

[26] S. R. Khan, B. Sharma, P. A. Chawla, and R. Bhatia. "Inductively Coupled Plasma Optical Emission Spectrometry (ICP-OES): a Powerful Analytical Technique for Elemental Analysis". In: *Food Analytical Methods* 15.3 (2022), pp. 666–688. DOI: 10.1007/s12161-021-02148-4.

[27] B. Raut. *chemistnotes*. 2022. URL: https://chemistnotes.com/analytical_chemistry/inductively-coupled-plasma-atomic-emission-spectroscopy-principle-instrumentation-and-7-reliable-applications/ (visited on 11/01/2022).

[28] M. Kaszuba, D. McKnight, M. T. Connah, F. K. McNeil-Watson, and U. Nobbmann. "Measuring sub nanometre sizes using dynamic light scattering". In: *Journal of Nanoparticle Research* 10.5 (2008), pp. 823–829. DOI: 10.1007/s11051-007-9317-4.

[29] M. Sartor. "Dynamic Light Scattering". In: (2003). URL: http://216.92.172.113/courses/phys39/light%5C%20scattering/DLS%5C%20LabView%5C%20UCSD.pdf.

[30] M. R. Zamani Kouhpanji and B. Stadler. “A Guideline for Effectively Synthesizing and Characterizing Magnetic Nanoparticles for Advancing Nanobiotechnology: A Review”. In: *Sensors* 20 (Apr. 2020), p. 2554. DOI: 10.3390/s20092554.

[31] C.Y. Tang and Z. Yang. “Chapter 8 - Transmission Electron Microscopy (TEM)”. In: *Membrane Characterization*. Ed. by N. Hilal, A. F. Ismail, T. Matsuura, and D. Oatley-Radcliffe. Elsevier, 2017, pp. 145–159. ISBN: 978-0-444-63776-5. DOI: https://doi.org/10.1016/B978-0-444-63776-5.00008-5. URL: https://www.sciencedirect.com/science/article/pii/B9780444637765000085.

[32] nuclear-power. *scintillation-counter-scintillation-detector*. URL: https://www.nuclear-power.com/nuclear-engineering/radiation-detection/scintillation-counter-scintillation-detector/ (visited on 11/01/2022).

[33] radiationanswers. *radiation: introduction detecting measuring: gamma-counter.* URL: https://www.radiationanswers.org/radiation-introduction/detecting-measuring/gamma-counter.html (visited on 11/01/2022).

[34] National library of medicine. *PubChem*. 2007. URL: https://pubchem.ncbi.nlm.nih.gov/compound/Poly_ethylene-glycol_-bis_carboxymethyl_-ether (visited on 01/14/2023).

[35] R.P. Fauzia. “Two-Step Radionuclide Tumor Targeting through Bioorthogonal Mechanism using SPIONs”. English. PhD thesis. Delft University of Technology, 2022. ISBN: 978-94-6384-295-2. DOI: 10.4233/uuid:9a06806c-a2ad-4588-bfad-0dd537867dbf.

[36] J. S. Suk, C. Xu, N. Kim, J. Hanes, and L. M. Ensign. “PEGylation as a strategy for improving nanoparticle-based drug and gene delivery”. In: *Adv Drug Deliv Rev* 99 (2015), pp. 28–51. DOI: 10.1016/j.addr.2015.09.012.

[37] Sigma-Aldrich. *Sigma-Aldrich*. URL: https://www.sigmaaldrich.com/NL/en/product/avanti/880135p (visited on 01/14/2023).

[38] E. Demangeat, M. Pédrot, A. Dia, M. Bouhnik-le-Coz, F. Grasset, K. Hanna, M. Kamagate, and F. Cabello-Hurtado. “Colloidal and chemical stabilities of iron oxide nanoparticles in aqueous solutions: the interplay of structural, chemical and environmental drivers”. In: *Environ. Sci.: Nano* 5 (4 2018), pp. 992–1001. DOI: 10.1039/C7EN01159H. URL: http://dx.doi.org/10.1039/C7EN01159H.

[39] G. A. Parks. “The Isoelectric Points of Solid Oxides, Solid Hydroxides, and Aqueous Hydroxo Complex Systems”. In: *Chemical Reviews* 65.2 (1965), pp. 177–198. DOI: 10.1021/cr60234a002. eprint: https://doi.org/10.1021/cr60234a002. URL: https://doi.org/10.1021/cr60234a002.

[40] D. D.L. Chung. “6 - Cement-Matrix Composites”. In: *Carbon Composites (Second Edition)*. Second Edition. Butterworth-Heinemann, 2017, pp. 333–386. ISBN: 978-0-12-804459-9. DOI: https://doi.org/10.1016/B978-0-12-804459-9.00006-3. URL: https://www.sciencedirect.com/science/article/pii/B9780128044599000063.

[41] M. Singh, R. Ramanathan, E. L.H. Mayes, S. Mašková, P. Svoboda, and V. Bansal. “One-pot synthesis of maghemite nanocrystals across aqueous and organic solvents for magnetic hyperthermia”. In: *Applied Materials Today* 12 (2018), pp. 250–259. ISSN: 2352-9407. DOI: https://doi.org/10.1016/j.apmt.2018.06.003. URL: https://www.sciencedirect.com/science/article/pii/S2352940718300921.

[42] A. P. LaGrow, M. Q. Besenhard, A. Hodzic, A. Sergides, L. K. Bogart, A. Gavriilidis, N. Thanh, and K. Thi. “Unravelling the growth mechanism of the co-precipitation of iron oxide nanoparticles with the aid of synchrotron X-Ray diffraction in solution”. In: *Nanoscale* 11 (14 2019), pp. 6620–6628. DOI: 10.1039/C9NR00531E. URL: http://dx.doi.org/10.1039/C9NR00531E.

[43] M. O. Besenhard, A. P. LaGrow, A. Hodzic, M. Kriechbaum, L. Panariello, G. Bais, K. Loizou, S. Damilos, M. M. Cruz, N. T. Kim Thanh, and A. Gavriilidis. “Co-precipitation synthesis of stable iron oxide nanoparticles with NaOH: New insights and continuous production via flow chemistry”. In: *Chemical Engineering Journal* 399 (2020), p. 125740. ISSN: 1385-8947. DOI: https://doi.org/10.1016/j.cej.2020.125740. URL: https://www.sciencedirect.com/science/article/pii/S1385894720318684.

[44] R. Ashraf, S. Riaz, Z. N. Kayani, and S. Naseem. “Effect of Calcination on Properties of ZnO Nanoparticles”. In: *Materials Today: Proceedings* 2.10, Part B (2015). International Conference on Solid State Physics 2013 (ICSSP’13), pp. 5468–5472. ISSN: 2214-7853. DOI: https://doi.org/10.1016/j.matpr.2015.11.071. URL: https://www.sciencedirect.com/science/article/pii/S2214785315010305.

[45] K. Ghandi, A. D. Findlater, Z. Mahimwalla, C. S. MacNeil, E. Awoonor-Williams, F. Zahariev, and M. S. Gordon. “Ultra-fast electron capture by electrosterically-stabilized gold nanoparticles”. In: *Nanoscale* 7 (27 2015), pp. 11545–11551. DOI: 10.1039/C5NR02291F. URL: http://dx.doi.org/10.1039/C5NR02291F.

A

Safety regulations for radioactive materials

Additional safety provisos were taken when working with ^{166}Dy and ^{166}Ho. The source used for this experiment was activated $Dy(NO_3)_3 \cdot 5\,H_2O$, the emissions were high energy β-particles and low energy γ-rays. The radioactive experiments were done in the fume hood. The fume hood was split up in a contaminated area and an uncontaminated area which was divided using lead bricks, for the γ-rays and plastic shielding, for the β-particles. The fume hood was closed when the source was open and the sliding window was used to perform the experiment. Furthermore, gloves were worn on the hand that was using the equipment in contact with the activity or potentially contaminated materials. The material and equipment needed to be disposed of correctly and when the experiment was done the area was monitored for contamination, if so it was cleaned [9].